ISSN 1391-0256

Journal of the Sri Lanka Association for the Advancement of Science

Volume 7 Issue 1, 2025

JSLAAS

Founded in 1944 and incorporated by the Act of Parliament No 11 of 1966.

Journal of the Sri Lanka Association for the Advancement of Science is a biannual publication. Selected research work from annual research sessions (based on scientific merit) as well as other research articles are invited to submit research manuscripts as per the guidelines provided by SLAAS. SLAAS members may also separately submit their papers for publication. The Journal can be accessed on-line to view and download the full text of the articles published respective to the volumes free of charge

Submission Manuscript

Only online submission, Web: https://journal.slaas.lk, e-ISSN: 2682-6992

Members of the Editorial Board

Exchanges: Please address all requests to the Secretary, *Sri Lanka Association for the Advancement of Science, "Vidya Mandiraya" 120/10, Wijerama Mawatha Colombo 07, Sri Lanka*

Table of Contents

Molecular docking of potential antifungal compounds from *Ulva fasciata*methanolic extract against *Pseudopestalotiopsistheae*

A. H. D. Alahakoon[1], B.K. D. M. Rodrigo[1], B.M. Chathuranga M. Balasooriya[2], H. M. Herath[1], R. P. Wanigatunge[1]*

[1]Department of Plant and Molecular Biology, Faculty of Science, University of Kelaniya, Sri Lanka
[2]School of Science, Mae Fah Luang University, Thailand.

ABSTRACT

Plant diseases caused by fungal pathogens significantly threaten global food security, accounting for nearly 40% of annual crop losses and incurring over US$220 billion in management costs worldwide. Among these, Pseudopestalotiopsistheae has emerged as notable phytopathogen in Sri Lanka, causing chlorosis in Solanum melongena. Its virulence is largely attributed to the secretion of pectinase enzymes, which degrade plant cell walls and facilitate host colonization. Excessive use of synthetic fungicides to manage such pathogens has led to environmental degradation, health risks, and the emergence of fungicide-resistant strains. Consequently, there is a growing interest in eco-friendly alternatives such as natural products derived from marine organisms. Marine macroalgae, particularly Ulva fasciata, commonly found in Thalpe reef, are known to produce a wide range of bioactive secondary metabolites with antifungal potential. In a previous study, methanolic extract of U. fasciata revealed numerous bioactive compounds with potential antifungal activity. The present studyaimed to evaluate the inhibitory potential of these compounds against the pectinase enzyme of P. theae using molecular docking, a powerful in silico approach for predicting interactions between small molecules and target proteins. The findings are expected to contribute to the development of sustainable, eco-friendly strategies for managing plant diseases, offering a cost-effective alternative to synthetic fungicides.This study highlights the potential of marine bioresources and computational tools in the discovery of novel antifungal agents targeting emerging phytopathogens.

Key words-Antifungal compounds, *Ulva fasciata*, Molecular docking, *Pseudopestalotiopsistheae*

INTRODUCTION

Approximately 40% of global crop production is lost each year due to attacks by pests and pathogens, including numerous bacterial and fungal species. To combat these plant diseases, more than US$ 220 billion is spent annually worldwide (FAO, 2022). Among emerging fungal pathogens, *Pseudopestalotiopsistheae*ishas been identified as a significant threat in Sri Lanka, causing chlorosis in *Solanum melongena* (Koshila *et al*., 2023). Its virulence is primarily attributed to secretion of extracellular pectinase enzymes which degrade plant cell walls and facilitate host colonization(Sopalun&Iamtham, 2020). Pectinases are a group of enzymes that hydrolyze glycosidic linkages in pectic polymers and are functionally categorized into polygalacturonases, pectin esterases, pectin lyases and pectate lyase (Arya*et al*., 2022). *Pseudopestalotiopsis*, *Neopestalotiopsis,* and *Pestalotiopsis* are closely related genera within the family Amphisphaeriaceaeand are known to cause various plant diseases, including cankers, shoot dieback, leaf spots, blights, severe chlorosis, and fruit

rot(Maharachchikumbura, 2014;Sane *et al*., 2019). Although chemical fungicides are widely used to control fungal infections,their excessive usage leads to serious environmental consequences, including contamination of aquatic ecosystems, residue accumulation in crops, and the emergence of resistant fungal strains. Moreover, fungicides pose risks to non-target organisms and human health(Goswami *et al*., 2018).

Biocontrol has been explored as a natural and sustainable alternative to chemical fungicides for managing various fungal infections in agriculture (Bubici*et al*., 2019). It involves mechanisms such as competition for space and nutrients, production of antifungal compounds and secondary metabolites (Rashad & Moussa, 2020), and the biological triggering of plant resistance (Hermosa *et al*., 2013). Plants, animals, and marine organisms are sources of natural products with inherent fungicidal activity (Dong *et al*., 2020). Marine macroalgae (seaweeds) are multicellular, eukaryotic and photosynthetic organisms known to be rich in bioactive compounds (Makkar *et al*., 2016).*Ulva fasciata*, a common macroalgae in Thalpe reef of Sri Lanka, showed potent antifungal activity against *P. theae*in a previous study through its methanolic extract (Rodrigo *et al*., 2025).Gas Chromatography-Mass Spectrometry (GC-MS) analysis of the extract revealed several potential antifungal compounds, includingPhenylephrine, Palmitic acid, 17-Octadecenal, 4-Hydroxy-2-butanone, Heptadecene and 3-Methoxyamphetamine. However, the specific mechanism by which these compounds inhibit the fungal activityremain unclear.

Molecular docking has become a valuable computational technique for exploring the therapeutic potential of natural products. This method simulates the interactions between bioactive compounds and target proteins, predicting binding affinity and interaction modes. By virtually testing thousands of molecules, molecular docking enables the identification of promising compounds efficiently, and cost-effectively, significantly reducing the need for extensive laboratory screening (Agu *et al*., 2023). In antifungal research, docking is particularly useful for identifying inhibitors of fungal enzymes or proteins that contribute to pathogenicity. It provides insights into how candidate molecules interact with target sites at the atomic level, assessing the strength and stability of these interactions (Hendra *et al*., 2024). Hence, the present study aimed to employ molecular docking techniques to investigate the binding interactions between the most potent bioactive compounds from the methanolic extract of *U. fasciata*and the extracellular enzymes of *P. theae*, with the objective of inhibiting their enzymatic activity. Though the fungus *P. theae* secretes pectinase as an extracellular enzyme to maintain its pathogenicity, the amino acid sequences or 3D structures of pectinase enzymes from *P. theae*are not currently available in databases. Therefore, the polygalacturonase sequence from *Pestalotiopsis* sp. NC0098 (KAI0138346.1) was used to construct a homology model for subsequent analysis as it is the only available related amino acid sequence in the databases.

METHODOLOGY

Homology modeling of polygalacturonase enzyme of *Pestalotiopsis* sp.

Polygalacturonase enzyme of *Pestalotiopsis* sp. NC0098 (KAI0138346.1) was used for generating the homology model as amino acid sequences or 3D structures of pectinases of the fungus *P. theae*were not available inthe NCBI GenBank protein database.

Polygalacturonaseamino acid sequence was searched against the Protein Data Bank (PDB) using the NCBI Protein BLAST tool to identify suitable homologous templates. Four template structures with

sequence identities ranging from 54.87% to 55.46% were retrieved. Multiple sequence alignment was performed using the CLUSTALW online tool and homology modeling was carried out using MODELLER software (version 10.1).From the generated models, the one with the lowest DOPE (Discrete Optimized Protein Energy) score was selected for further analysis, as lower DOPE scores indicate higher model reliability (Selvam *et al*., 2017). The selected model was further refined in MODELLER, and energy minimization was performed using the GROMOS simulation package within Swiss-PdbViewer. Model validation was conducted using several structure assessment tools: PROCHECK, Verify3D, and ERRAT to assess stereochemical quality and 3D structure compatibility. Additionally, PROSA was used to calculate the Z-score, and the QMEAN score was evaluated using its corresponding web server to assess the overall quality and stability of the predicted structure (Selvam *et al*., 2017).

Active compound identification in the *U. fasciata*– methanolicextract

Potential antifungal compounds present in *U. fasciata*-methanolic extract were identified by GC-MS analysis as described by Kamal *et al*. (2011) in our previous study (Rodrigo *et al*., 2025).

Molecular docking

Molecular docking analysis was carried out using the AutoDock Vina software (Version 1.1.2). The homology-modeled polygalacturonase protein served as the receptor, and the receptor was prepared using Auto Dock Tools software (Version 1.5.7). The molecule was checked for adding polar H molecules and missing amino acid residues. Kollman charges were added to the molecule by equally distributing the charge across the protein surface (Phosrithong & Ungwitayatorn, 2010).

Ligand structures were based on the chemical compounds previously identified through GC-MS analysis (Rodrigo *et al*., 2025). Structures of the selected chemical molecules were obtained from the PubChem database, and energy was minimized using AVOGADRO software (Version 1.2.0). The minimized structures were then converted into a Protein Data Bank file format (pdb) using Open Babel software (Version 3.1.1). Potential ligand-binding pockets on the receptor were identified using the DoGSiteScorertool of the ProteinsPlus server. The binding pocket with the highest drug score value was selected for docking the ligands (Selvam *et al*., 2017). Nine independent docking runs were carried out for each ligand and the best binding mode with the lowest (most negative) binding free energy was selected as the best conformation (Phosrithong & Ungwitayatorn, 2010).

RESULTS AND DISCUSSION

Homology modeling of the Polygalacturonase enzyme

The extracellular enzymes are the pathogenicity determinant factors in many plant pathogens as they facilitate host invasion by degrading plant cell wall components. Enzymes are proteins that catalyze chemical reactions in living organisms, and their activity can be inhibited by certain bioactive compounds. Marine algae are known to produce diverse secondary metabolites capable of interferingwith such enzymes present in the plant pathogenic fungi and lead to the inhibition of their activity (Agu *et al*., 2023).

In this study, a homology model of the polygalacturonase enzyme was generated with 4 similar crystal structures available in the protein data bank using the MODELLER software (Figure 1). Then the loops of the structures were refined, and energy was minimized. The best model was evaluated using online servers of PROCHECK, Verfiy3D, ERRAT, PROSA, and QMEAN.

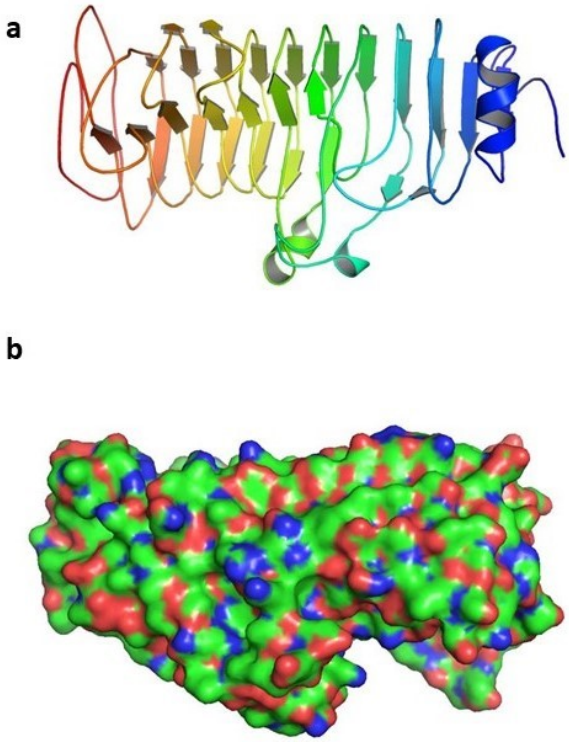

Figure 1. Homology model of polygalacturonase enzyme of *Pestalotiopsis* sp. (a) cartoon diagram (b) surface view diagram of the energy-minimized protein model

Each tool assesses different aspects of protein structure quality. PROCHECK evaluates the stereochemical quality of a protein structure including parameters like bond lengths, bond angles and planarity using Ramachandran plot analysis (Figure 2) (Wlodawer, 2017). A high percentage of residues in the most favored regions is indicative of a well-refined model. Values above 90% are considered excellent, while those exceeding 80% are generally acceptable. In this study, PROCHECK analysis revealed that 84.4% of residues (Table 1) were located in the most favoured regions of the Ramachandran plot, which falls within the acceptable range and is comparable to previous models developed for *Aspergillus niger*enzymes (Gundampati*et al*., 2012).This suggests that the overall stereochemical quality of the model is acceptable. Furthermore, no residues were observed in the generally allowed or disallowed regions (0.0%), proving the reliability of the model. The additional allowed regions (%) ideally range between 1–15%, and this model exhibited 15.6% (Table 1), which, although at the upper threshold, still falls within the acceptable range. This value is slightly higher than the percentage reported in the additionally allowed regions for *A. niger* (Gundampati*et al*., 2012). However, the overall results support the structural validity of the predicted model.

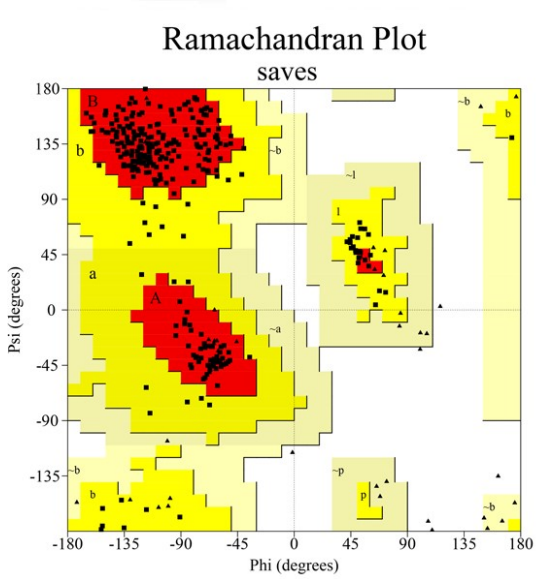

Figure 2. Ramachandran plot of the model

Table 1. Model evaluation results of PROCHECK, Verfiy3D, and ERRAT

Program	PROCHECK				Verfiy3D	ERRAT
	Most favored regions	Additional allowed regions	Generally allowed regions	Disallowed regions	3D-ID Score	Quality Factor
Value	84.4%	15.6%	0.0%	0.0%	81.07%	76.03%

Table 2. Model evaluation results of QMEAN and PROSA

Program	QMEAN	PROSA
	QMEAN4 Value	Z-Score
Value	-0.46	-6.49

Verfiy3D assesses the compatibility of the 3D model with its own amino acid sequence by assigning a 3D environment score to each residue and compares it with known preferences based on experimentally determined structures (Eisenberg *et al*., 1997).A model is generally considered reliable if a 3D-1D scoreis more than 80%.In this study, Verfy3D analysis showed 81.07% of the residues had an acceptable 3D-1D score (Table 1), indicating that the residue environments are biochemically plausible and structurally consistent.

ERRAT analyzes non-bonded atomic interactions to identify statistical deviations by comparing the input protein structure to high-resolution crystallographic data, and it computes an overall error function that reflects the model's reliability. A quality factor above 90% is indicative of an excellent model, while values between 70% and 90% are generally considered acceptable. In this study, the model achieved 76.03% quality factor,suggesting that the non-bonded interactions are largely consistent with those found in experimentally validated structures. Although this value is slightly lower

than the 83.97% reported for *Trichoderma longibrachiatum* (Tambol*iet al*., 2017), it remains within the acceptable range for functional docking studies, thereby supporting the structural plausibility of the model.

QMEAN (Qualitative Model Energy Analysis) is another important tool used to assess the quality of predicted protein structures. It is a composite scoring function that evaluates local geometry (torsion angles, solvation, hydrogen bonding), long-range interactions and agreement with high-resolution structures (Benkert *et al*., 2008). The QMEAN score typically ranges from 0 to –4, with values closer to 0 indicating a high-quality model. In this study, the QMEAN score was -0.46 (Table 2), which is close to 0 and comparable to the QMEAM values reported for *Aspergillus ficuum*, where scores were -3 or higher (Chikkerur*et al*., 2018).This suggests that the modeled structure is of good quality and comparable to experimentally determined protein structures.

PROSA provides a Z-score that indicated the energy separation of the native and average of the misfolds in the units of standard deviation (Heydari-Zarnagh*et al*., 2015). If z-score falls –4 to –10 typically indicates that global structure resembles real proteins. In our study, the PROSA Z-score was –6.49 (Table 2), which falls well within this acceptable range, suggesting that the modeled structure is realistic and reliable. This is comparable to the Z-score reported in the PROSA analysis for *Trichoderma longibrachiatum*which had a Z-score of -6.78 (Tambol*iet al*., 2017).

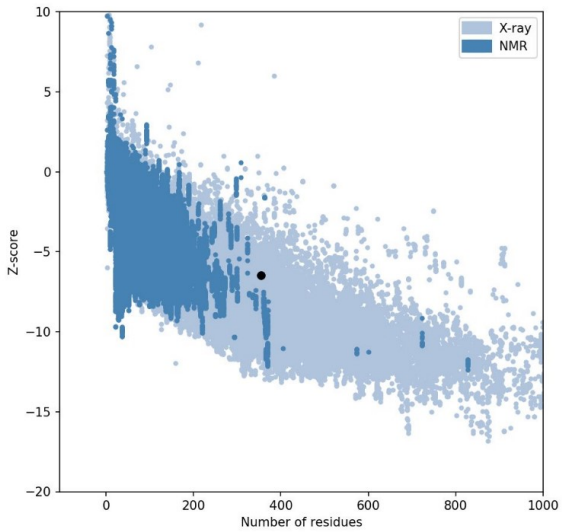

Figure 3. ProSA Z-score plot of the model. The value of Z-score is highlighted as a black dot and is in the range of native conformations

This multi-angle validation is essential to build trust in the accuracy of a predicted or experimentally determined protein model before using it in downstream applications like molecular docking, drug design, or structural biology research. The scores received for these tests indicate that the model generated was of good quality, and it has higher reliability (Selvam *et al*., 2017).

Biologically active compounds in the *U. fasciata*– methanolic extract

Nine different chemical compounds were identified in our previous study by Rodrigo *et al*. (2025) using GC-MS analysis (Table 3). Various aromatic and non-aromatic compounds were found in different abundances (Figure 3). The most abundant compounds in the extract were 4-hydroxy-2-butanone (30.75%) followed by hydroxylamine/methylamine (37.37%).

Table 3. Chemical compounds identified from of *U. fasciata*-methanolic extract

Compound	Retention time (min)	Compound ID	Molecular formula	% of total
Phenylephrine 3-Methoxyamphetamine	01.10	6041 152234	$C_9H_{13}NO_2$ $C_{10}H_{15}NO$	00.12
Hydroxylamine Methylamine	01.14	787 6329	H_3NO CH_5N	37.37
4-Hydroxy-2-butanone	01.15	111509	$C_4H_8O_2$	40.75
17-Octadecenal	02.33	41922	$C_{18}H_{34}O$	01.75
Palmitic acid	16.05	985	$C_{16}H_{32}O_2$	00.57
Bicyclo[3.1.1]heptane, 2,6,6-trimethyl-,(1alpha,2beta,5alpha)	16.80	12314300	$C_{10}H_{18}$	0.57
1,2-Benzisothiazol-3-amine	25.678	89966	$C_7H_6N_2S$	0.03

When considering previously published data, variations in chemical composition have been reported even among extracts from the same species (Abbassy*et al*., 2014; Shobier*et al*., 2016). These differences are likely due to variations in secondary metabolites profiles, which can be influenced by factors such as geographical locations, environmental conditions, and the development stage of the algae.

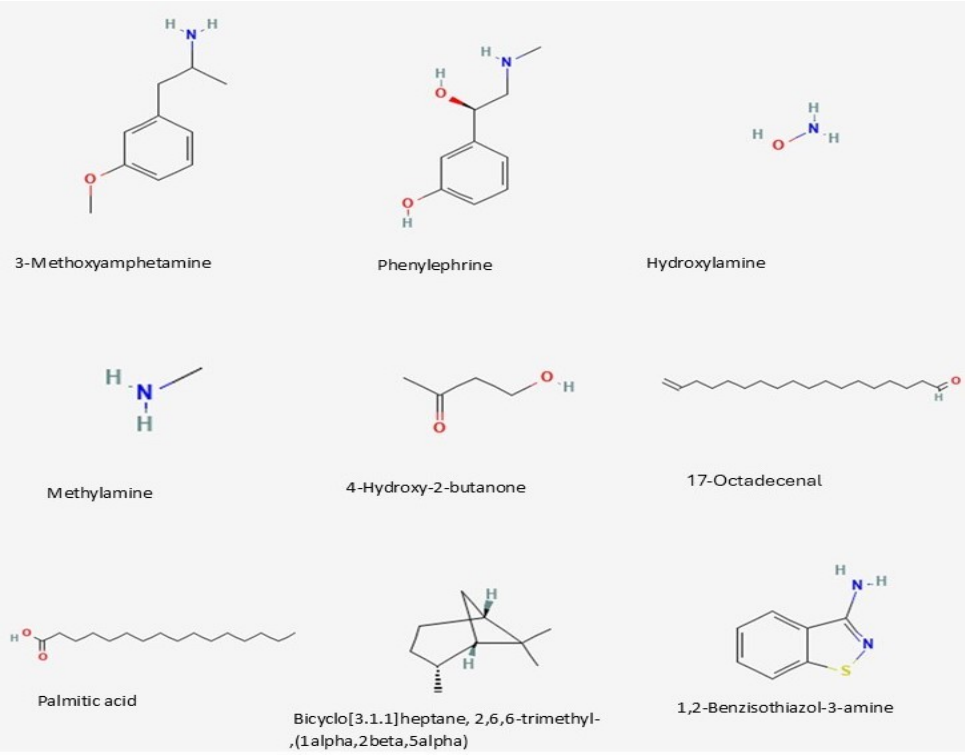

Figure 4. Structures of the studied bioactive compounds in *U. fasciata*-methanolic extract

Palmitic acid (RT=18.056 min) was detected in this study, and it has commonly been reported in previous studies of *Ulva*-methanol extract (Abbassy*et al*., 2014; Barot *et al*., 2016; Shobier*et al*., 2016). The exact mechanisms by which antifungal compounds derived from macro algae effect fungal growth inhibition are still not fully understood. But several hypotheses have been proposed. Compounds found in algal extracts may exert antifungal effects through multiple mechanisms, including disruption of cell wall and membrane integrity, interference withkey intracellular components like the nucleus and mitochondria, inhibition of protein synthesis and enzymatic functions and impairment of the mitochondrial respiratory chain. These actions collectively destabilize cellular homeostasis, ultimately reducing the fungal cell's viability and lifespan (Lopes *et al*., 2013). Additionally, certain fatty acids from macroalgae exhibit antifungal activity by incorporating into the fungal membrane, altering its fluidity and permeability, and reorganizing its structure, which ultimately leads to cell death (Avis & Bélanger, 2001). Molecular docking can predict the binding site and the strength of the interaction between these algal chemical compounds and the fungal extracellular enzymes, which can help in understanding the mechanism of action.

Molecular docking

If the methanolic extract of*U.fasciata*- could significantly inhibit fungal activity, it is plausible that its bioactive compounds may have the ability to bind with extracellular enzymes and inhibit their function. To check this possibility, an *in-silico* analysis was carried out. Potential ligand binding sites of the target protein model were identified using the DoGSiteScorertool which predicts druggable pockets based on protein structure analysis. The best binding pocket (Figure 4) was selected based on its highest drug score value of 0.81. The volume of the pocket was 1422.87 Å 3 and the surface area was 1413.39 Å 2. It comprised 322 atoms and featured 82 H-bond acceptor sites and 31 H-bond donor sites.

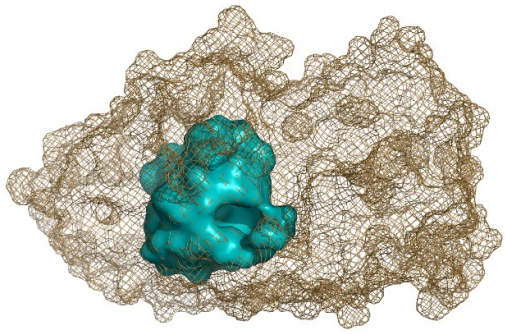

Figure 5. The best possible ligand-binding pocket of the protein model (green color area)

The 3D structures of nine compounds identified from GC-MS analysis were prepared as ligands for molecular docking. Docking simulations were performed using AutoDock Vina, which predicted the binding affinities of all nine ligands. Each ligand was docked into the selected binding pocket of the target protein model. All nine ligands successfully bound within the selected pocket, with predicted binding free energies ranging from –2.2 to –5.8 kcal/mol (Table 4).

Binding free energy (kcal/mol) provides a numerical estimate of the strength of interaction between a ligand and a target protein, where more negative values indicate stronger predicted binding affinities. Generally, values below –7.0 kcal/mol indicate strong binding potential, –5.0 to –7.0 kcal/mol suggest

moderate but stable binding interactions, and –3.0 to –5.0 kcal/mol indicate relatively weaker binding (Meng *et al*., 2011).

Table 4. Best docking score of ligands with the protein model

Ligand name	Docking score of the best conformation (kcal/mol)
1,2-Benzisothiazol-3-amine	-5.0
3-Methoxyamphetamine	-5.0
4-Hydroxy-2-butanone	-3.6
17-Octadecenal	-4.4
Bicyclo[3.1.1]heptane, 2,6,6-trimethyl-,(1alpha,2beta,5alpha)	-5.8
Hydroxylamine	-3.7
Methylamine	-2.2
Palmitic acid	-4.7
Phenylephrine	-5.7

The highest docking score was observed forBicyclo[3.1.1]heptane,2,6,6 trimethyl,(1alpha,2beta,5alpha) (-5.8 kcal/mol), followed by Phenylephrine (-5.7 kcal/mol), revealing stronger predicted binding affinities compared to the other ligands and suggesting a greater potential to form stable interactions with the extracellular enzyme (Selvam *et al*., 2017). Figures 5 and 6 illustrate the docking complexes and the interactions between these ligands and amino acid residue within the binding pocket. Notably, both ligands form multiple hydrogen bonds and hydrophobic interactions, which are critical for stabilizing ligand-protein complexes. These findings suggest that the compounds may inhibit enzymatic activity by occupying or altering the confirmation of the active site, thereby preventing substrate binding or catalytic function.

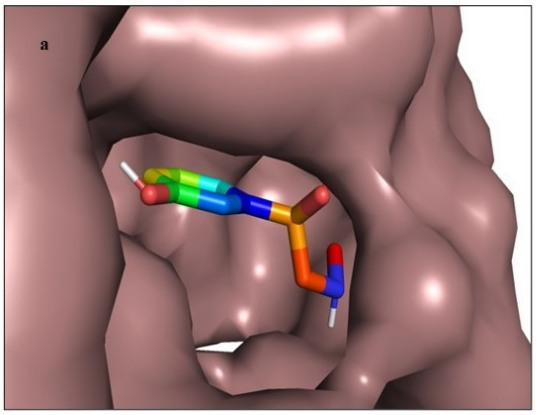

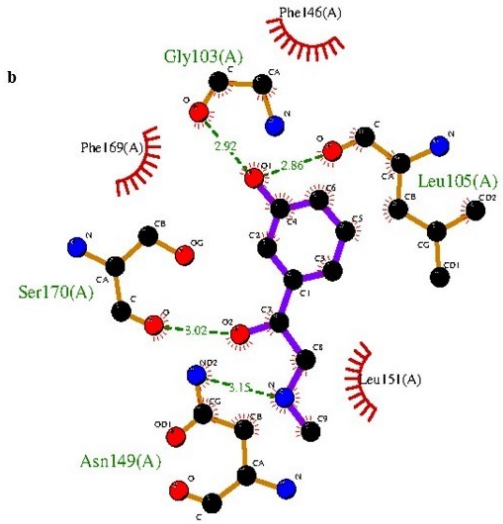

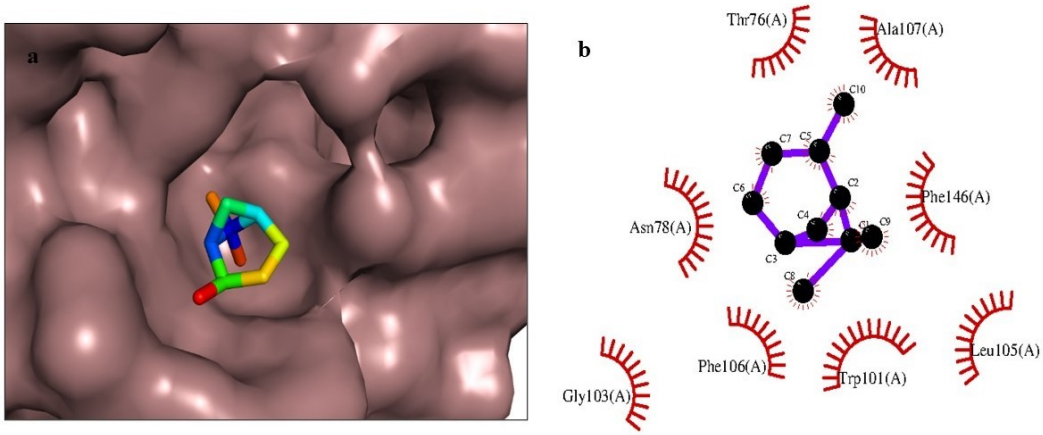

Figure 6. Docking complex and interactions of bicyclo[3.1.1]heptane,2,6,6-trimethyl-,(1alpha,2beta,5alpha) and the amino acids of the model for, (a) 3D structure (b) 2D structure

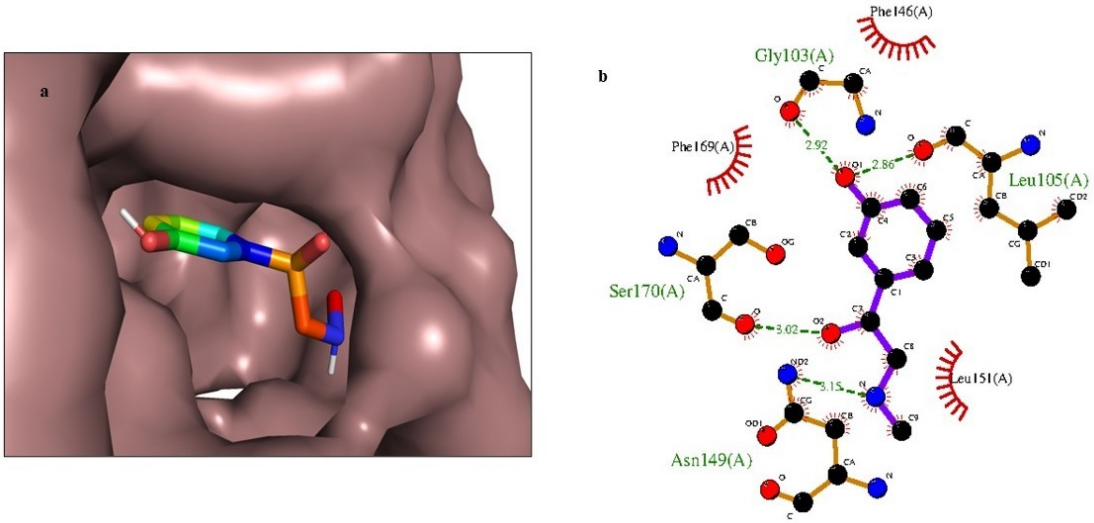

Figure 7. Docking complex and interactions of Phenylephrine and the amino acids of the model for, (a) 3D structure (b) 2D structure

Furthermore, compounds such as 1,2-Benzisothiazol-3-amine (-5.0 kcal/mol) and 3-Methoxyamphetamine (-5.0 kcal/mol) showed moderately strong binding affinities, suggesting they may contribute synergistically to the overall antifungal activity of the extract. The presence of multiple bioactive compounds with diverse binding profiles may enable the extract to target a broader range of fungal enzymes, thereby enhancing its overall efficacy. Thesefindings showed the potential of marine macroalgae-derived compounds as enzyme inhibitors, and support their promise as a sustainable source for development of novel antifungal agents.

CONCLUSION

In this study, molecular docking simulations were employed to identify potential antifungal targets of compounds present in the *U. fasciata*-methanol extract. The docked ligands demonstratednotable binding interactions with the polygalacturonase enzyme of *Pestalotiopsis*, a key pathogenic determinant. Among the tested compounds, Bicyclo[3.1.1]heptane,2,6,6-trimethyl-

,(1alpha,2beta,5alpha) (-5.8 kcal/mol) and Phenylephrine (-5.7 kcal/mol) exhibited the highest binding affinities, indicating stable and moderate interactions with the enzyme. These findings provide preliminary evidence supporting the antifungal potential of *U. fasciata* metabolites and highlight their possible applications in developing sustainable, macroalgae-derived fungicides for crop protection against fungal pathogens.

ACKNOWLEDHMENT

This research was funded by the National Research Council of Sri Lanka (IDG 22-062), and Research Council of University of Kelaniya (RC/2025/PPRP02).

REFERENCES

[1] Abbassy, M.A., Marzouk, M.A., Rabea, E.I. & Abd-Elnabi, A.D. (2014). Insecticidal and fungicidal activity of *Ulva lactuca* Linnaeus (Chlorophyta) extracts and their fractions. *Annual Research & Review in Biology*, *4*(13), 2252-2262. DOI: 10.9734/ARRB/2014/9511

[2] Agu, P.C., Afiukwa, C.A., Orji, O.U., Ezeh, E.M., Ofoke, I.E., Ogbu, C.O., Ugwuja, E.I. & Aja, P.M. (2023). Molecular docking as a tool for the discovery of molecular targets of nutraceuticals in diseases management. *Scientific Reports, 13*, 13398. https://doi.org/10.1038/s41598-023-40160-2

[3] Arya, P.S., Yagnik, S.M., Rajput, K.N., Panchal, R.R. & Raval, V.H. (2022). Valorization of agro-food wastes: Ease of concomitant-enzymes production with application in food and biofuel industries, *Bioresource Technology*, *361*, 127738, ISSN 0960-8524. https://doi.org/10.1016/j.biortech.2022.127738.

[4] Avis, T.J. & Bélanger, R.R. (2001). Specificity and mode of action of the antifungal fatty acid cis-9 heptadecenoic acid produced by *Pseudozymaflocculosa*. *Applied EnvironmentalMicrobiology, 67*, 956-960. https://doi.org/10.1128/AEM.67.2.956-960.2001

[5] Barot, M., Kumar, N.J.I. & Kumar, R.N. (2016). Bioactive compounds and antifungal activity of three different seaweed species *Ulva lactuca*, *Sargassum tenerrimum* and *Laurencia obtusa* collected from Okha coast, Western India. *Journal of Coastal Life Medicine*, *4*(4), 284-289. 10.12980/jclm.4.2016J5-185

[6] Benkert, P., Tosatto, S. C. & Schomburg, D. (2008). QMEAN: A comprehensive scoring function for model quality assessment. *Proteins: Structure, Function, and Bioinformatics*, *71*(1), 261-277. https://doi.org/10.1002/prot.21715

[7] Bubici, G., Kaushal, M., Prigigallo, M.I., Gomez-Lama Cabanas, C. & Mercado-Blanco, J. (2019). Biological control agents against Fusarium wilt of banana. *Frontiers in Microbiology*, *10*, 616. https://doi.org/10.3389/fmicb.2019.00616

[8] Chikkerur, J., Samanta, A. K., Dhali, A., Kolte, A. P., Roy, S., & Maria, P. (2018). *In Silico* evaluation and identification of fungi capable of producing endo-inulinase enzyme. *PloS one*, *13*(7), e0200607. https://doi.org/10.1371/journal.pone.0200607

[9] Dong, J., Huang, S.S., Hao, Y.N., Wang, Z.W., Liu, Y.X., Li, Y.Q. & Wang, Q.M. (2020). Marine-natural-products for biocides development: first discovery of meridianin alkaloids as antiviral and anti-phytopathogenic-fungus agents. *Pest Management Science*. *76*(10), 3369-3376. https://doi.org/10.1002/ps.5690

[10] Eisenberg, D., Lüthy, R., & Bowie, J. U. (1997). VERIFY3D: Assessment of protein models with three-dimensional profiles. Macromolecular Crystallography Part B, *277*:396-404. https://doi.org/10.1016/S0076-6879(97)77022-8

[11] Food and Agriculture Organization of the United Nations (2022). FAO's Plant Production and Protection Division. Rome. https://doi.org/10.4060/cc2447en

[12] Goswami, S. K., Singh, V., Chakdar, H., & Choudhary, P. (2018). Harmful effects of fungicides-Current status. *International Journal of Agriculture, Environment and Biotechnology*, *11*(779), 1011-1019.

[13] Gundampati, R. K., Chikati, R., Kumari, M., Sharma, A., Pratyush, D. D., Jagannadham, M. V., Kumar, C. S. & Debnath Das, M. (2012). Protein-protein docking on molecular models of Aspergillus niger RNase and human actin: novel target for anticancer therapeutics. *Journal of molecular modeling*, *18*(2), 653-662. https://doi.org/10.1007/s00894-011-1078-4

[14] Hendra, R., Agustha, A., Frimayanti, N., Abdulah, R., & Teruna, H. Y. (2024). Antifungal Potential of Secondary Metabolites Derived from *Arcangelisia flava* (L.) Merr.: An Analysis of *In Silico* Enzymatic Inhibition and *In Vitro* Efficacy against *Candida* Species. *Molecules*, *29*(10), 2373. https://doi.org/10.3390/molecules29102373

[15] Hermosa, R., Rubio, M.B., Cardoza, R.E., Nicolas, C., Monte, E. & Gutierrez, S. (2013). The contribution of *Trichoderma* to balancing the costs of plant growth and defense. *International Microbiology*, *16*(2):69-80. 10.2436/20.1501.01.181

[16] Heydari-Zarnagh, H., Hassanpour, K. &Rasaee, M. J. (2015). Constructing chimeric antigen for precise screening of HTLV-I infection. *Iranian Journal of Allergy, Asthma and Immunology*, *14*(4):427-436. https://doi.org/10.3390/molecules29102373

[17] Kamal, G.M., Anwar, F., Hussain, A.I., Sarri, N. & Ashraf, M.Y. (2011). Yield and chemical composition of *Citrus* essential oils as affected by drying pretreatment of peels. *International Food Research Journal*, *18*(4), 1275-1282.

[18] Koshila, H. V. A. S., Wanigatunge, R. P., Dias, R. K. S., & Edirisinghe, P. (2023). Morphological Characterization and Molecular Identification of Three Fungal Pathogens Isolated from *Solanum melongena* L. in Sri Lanka. *Journal of Agricultural Sciences–Sri Lanka*, *18*(2). 251-260. 10.4038/jas.v18i2.10257

[19] Lopes, G., Pinto, E., Andrade, P.B. & Valentao, P. (2013). Antifungal activity of phlorotannins against dermatophytes and yeasts: approaches to the mechanism of action and influence on *Candida albicans* virulence factor. *PloS One*, *8*(8), e72203. https://doi.org/10.1371/journal.388pone.0072203

[20] Maharachchikumbura, S. S. N., Hyde, K.D., Groenewald, J. Z., Xu, J. & Crous, P.W. (2014). *Pestalotiopsis* revisited. *Studies in Mycology*. *79*(1), 121–186. 10.1016/j.simyco.2014.09.005

[21] Makkar, H.P.S., Tran, G., Giger-Reverdin, V.H.S., Lessire, M., Lebas, F. & Ankers, P. (2016). Seaweeds for livestock diets: A review. *Animal Feed Science and Technology*, *212*, 1-17. http://dx.doi.org/10.1016/j.anifeedsci.2015.09.018

[22] Meng, X. Y., Zhang, H. X., Mezei, M., & Cui, M. (2011). Molecular docking: A powerful approach for structure-based drug discovery. *Current Computer-Aided Drug Design*, 7(2), 146–157. https://doi.org/10.2174/157340911795677602

[23] Phosrithong, N. &Ungwitayatorn, J. (2010). Molecular docking study on anticancer activity of plant-derived natural products. *Medicinal chemistry research*, *19*(8), 817-835. https://doi.org/10.1007/s00044-009-9233-5

[24] Rashad, Y.M. & Moussa, T.A.A. (2020). Biocontrol agents for fungal plant diseases management. In: El-Wakeil, N., Saleh, M., Abuhashim, M. (Eds.), Cottage Industry of Biocontrol Agents and Their Applications (pp. 101–122). Springer, Cham, Switzerland.

[25] Rodrigo, B.K. D. M., Alahakoon, A. H. D., Balasooriya, B.M.C. M., Edirisinghe, P., Herath, H. M., &Wanigatunge, R. P. (2025). Antifungal activity of extracts from *Ulva*, *Sargassum*, and *Gracilaria* against three fungal pathogens and GC-MS analysis of the most effective extracts. *International Journal of Secondary Metabolite*, *12*(2), 331-342. https://doi.org/10.21448/ijsm.1506431

[26] Sane, S., Sharma, S., Konduri, R. & Fernandes, M. (2019). Emerging corneal pathogens: First report of: *Pseudopestalotiopsistheae*: keratitis. *Indian Journal of Ophthalmology*, *67*(1), 150-152. http://dx.doi.org/10.4103/ijo.IJO_791_18

[27] Selvam, K., Senbagam, D., Selvankumar, T., Sudhakar, C., Kamala-Kannan, S., Senthilkumar, B. &Govarthanan, M. (2017). Cellulase enzyme: homology modeling, binding site identification and molecular docking. *Journal of Molecular Structure*, *1150*, 61-67. https://doi.org/10.1016/j.molstruc.2017.08.067

[28] Shobier, A.H., Ghani, S.A.A. & Barakat, K.M. (2016). GC/MS spectroscopic approach and antifungal potential of bioactive extracts produced by marine macroalgae. *The Egyptian Journal of Aquatic Research*, *42*(3), 289-299. https://doi.org/10.1016/j.ejar.2016.07.003

[29] Sopalun, K. &Iamtham, S. (2020). Isolation and screening of extracellular enzymatic activity of endophytic fungi isolated from Thai orchids. *South African Journal of Botany*, *134*, 273-279. https://doi.org/10.1016/j.sajb.2020.02.005

[30] Tamboli, A. S., Waghmare, P. R., Khandare, R. V., &Govindwar, S. P. (2017). Comparative analyses of enzymatic activity, structural study and docking of fungal cellulases. *Gene Reports*, *9*, 54-60. 10.1016/j.genrep.2017.08.008

[31] Wlodawer, A. (2017). Stereochemistry and Validation of Macromolecular Structures. *Methods in Molecular Biology, 1607*, 595-610. https://doi.org/10.1007/978-1-4939-7000-1_24

Dosimetric Impact on IMRT Plans of Altering Per Control Point Statistical Uncertainty in Monaco TPS

K. L. I. Gunawardhana*[1], J. Jeyasugiththan[2], P. De Silva[1] and D. Satharasinghe[2]

[1]Department of Radiotherapy, National Hospital Galle, Sri Lanka

[2]Department of Nuclear Science, University of Colombo, Colombo, 00300, Sri Lanka

ABSTRACT

Intensity-Modulated Radiation Therapy (IMRT) uses computer-controlled linear accelerators to deliver precise radiation doses to benign or malignant tumors or specific areas within tumors while minimizing exposure to healthy tissues and organs at risk. The purpose of this study is to evaluate the dosimetric impact on IMRT plans of changing the per control point Statistical Uncertainty (SU) from 1% to 6% in 1% increments using the Monaco Treatment Planning System (TPS) for three different diagnoses: Larynx, Oesophagus, and Prostate. The per control point SU is a key factor in determining dose calculation accuracy and calculation time. In this study, 54 IMRT plans were generated by varying the per control point SU as 1%, 2%, 3%, 4%, 5%, and 6%, using nine patients for each diagnosis. Dosimetric indices, including Conformity Index, Heterogeneity Index, Target Dose (PTV), Organ At Risk doses, Dose Calculation Time, Treatment Delivery results, and Dose Volume Histogram, were used to evaluate the generated plans. No significant differences were observed across all dosimetric indices, and an exponential relationship was found between Dose Calculation Time and the per control point SU. For IMRT plans, a 3% per Control Point SU is acceptable, providing shorter and adequately accurate dose calculation times without compromising plan quality or deliverability.

Keywords: Radiotherapy, IMRT, dosimetric impact, Per Control Point, Statistical Uncertainty

* isuru.gunawardhana@phys.cmb.ac.lk

INTRODUCTION

Radiotherapy is a medical treatment that uses high doses of radiation (gamma rays, high-energy X-rays, and Electrons) to kill or damage benign and malignant tumors (Hall & Giaccia, 2019). It is a crucial component of cancer treatment and is employed either as radiotherapy itself or in combination with surgery, chemotherapy, or immunotherapy (Delaney, Jacob, Featherstone, & Barton, 2005). Radiotherapy can be given inside or outside of our bodies. The most common kind is External Beam Radiation Therapy (EBRT). It uses a large machine called a Linear Accelerator (Linac) to treat cancer patients using high-energy X-rays and electrons. At present, there are other advanced types of machines used for radiotherapy treatment too. Such as Tomotherapy machine, Cyberknife machine, MR-Lianc, PET-Linac, ProBeam machine, GammaKnife machine, and ZAP-X machine (Palta & Mackie, 2011). There are ordinary and advanced treatment techniques currently used in the oncology field using those advanced machines. Such as three-dimensional conformal Radiotherapy (3DCRT), Intensity-Modulated Radiation Therapy (IMRT), Image-Guided Radiation Therapy (IGRT), Volumetric Modulated Arc Therapy (VMAT), Stereotactic Body Radiation Therapy (SBRT), Proton Therapy, and Adaptive Radiation Therapy (ART) (Khan & Gibbons, 2014). Apart from those machines, the cobalt 60 machine is used to treat cancer patients using Gamma-rays, and it is an older version of a raditherapy treatment machine (Podgorsak, 2005).

Intensity-Modulated Radiation Therapy, also called IMRT, is an advanced type of radiation therapy technique, and it is an inverse planning technique (Bortfeld, 2006). Inverse planning is a technique that uses a computer program to automatically achieve a treatment plan that has an optimal merit. Here, it is less dependent on the geometric parameters but more on the specification of volumes of tumor targets and organs at risk, as well as their dose constraints. IMRT uses computer-controlled linear accelerators to deliver precise radiation doses to a benign or malignant tumor or specific areas within the tumor. IMRT allows for the radiation dose to conform more precisely to the three-dimensional (3-D) shape of the tumor by modulating or controlling the intensity of the radiation beam in multiple small segments. Also, IMRT allows higher radiation doses to be focused on the tumor while minimizing the dose to surrounding normal critical structures. Because the ratio of normal tissue dose to tumor dose is reduced to a minimum with the IMRT approach, higher and more effective radiation doses can safely be delivered to tumors with fewer side effects compared with conventional radiotherapy techniques. IMRT also has the potential to reduce treatment toxicity, even when doses are not increased. Due to its complexity, IMRT does require slightly longer daily treatment times, additional planning, and safety checks before starting the patient treatment (IMRT Patient Specific Quality Assurance) when compared with conventional radiotherapy (Gupta, Agarwal, Ghosh-Laskar, & Shrivastava, 2009).

IMRT was first conceptualised in the 1960s (Intensity Modulated Radiation Therapy Collaborative Working Group, 2001). Although the concept of IMRT and early algorithms for planning were developed in Sweden, clinical application did not begin until a fully integrated IMRT planning and delivery system, namely, the NOMOS Peacock system, was invented and commissioned in 1993 by the collaborated effort between NOMOS and Baylor College of Medicine/the Methodist Hospital (Houston, TX, USA) (Mohan, 2005). After obtaining investigational device exemptions and protocol approval by Baylor's Investigational Review Board, the first patient with brain metastases was to have three brain tumors treated simultaneously using IMRT in September 1993 (Lawrence & Cox, 1995). In 1994, the NOMOS Peacock system was introduced as the first commercial IMRT delivery unit. The Peacock system required the use of a beam modulation device known as a dynamic multivane intensity-

modulating collimator (MIMiC). This particular form of IMRT, called serial tomotherapy, could be treated by a continuously rotating gantry (Carol, 1995). Step and shoot IMRT represents another commonly used technique whereby multiple static beams are subdivided into 'segments' (LoSasso, Chui, & Ling, 1998). In the sliding window technique (dynamic Multileaf Collimator- dMLC), a window defined by the MLC leaves sweeps across the treatment field at variable speed, while the monitor units are delivered continuously (Zhang et al., 2007).

Dose calculation accuracy in IMRT is an important and crucial factor to prevent mistreatment of radiation treatment delivery using linear accelerator machines (Papiez & Langer, 2006). Among the commercially available dose calculation algorithms, Monte Carlo (MC) is considered to be potentially more accurate and complex than others. Although MC dose calculation algorithms are recognized as the most accurate dose computation algorithms for treatment planning, their inherent Statistical Uncertainty (SU) determines the accuracy of the dose calculation and the time span of the dose calculation (Taleei & Tabrizi, 2019). The SU decreases inversely with the square root of the time span of the dose calculation. By decreasing the SU, one can increase the dose calculation accuracy. But the SU decreases, resulting in a significant increase in the time span of the dose calculation. Therefore, it should be a compromise between the SU and the dose calculation accuracy, with a suitable time span for the dose calculation in IMRT planning. Therefore, by studying this, it is possible to get an idea about how to optimize the accuracy of the dose calculation and the SU with a suitable time span of the dose calculation in IMRT planning (Chetty et al., 2007).

There are many Treatment Planning Systems (TPSs) that can be used to develop IMRT plans, utilizing their own dose calculation algorithm (Vassiliev et al., 2010). The Elekta's Monaco TPS is one of the most powerful tool that bring increased automation, intelligent workflows, and high-quality treatment planning to a wide range of radiotherapy treatment delivery systems.

The Monaco TPS combines the MC dose calculation algorithm with robust optimization tools to provide high-quality radiotherapy treatment plans for IMRT, VMAT, and SBRT (Goodall & Ebert, 2020). The Monaco 5.11.02 TPS used two kinds of SUs. Such as per control point SU and per calculation SU, and the planner can manually select one of them. In this research, we used a per control point SU to generate IMRT plans. Also, the Monaco 5.11.02 TPS has an option to choose different percentage values between 0.1% - 10 % (Kry et al., 2019). In the per control point SU, the percentage uncertainty is based on the per voxel on a per segment. Also, the uncertainty was not the same in all voxels. The low-dose voxels in the peripheral regions of the patient had a higher uncertainty of dose than the voxels in the region of the maximum dose (PTV) (Keall, Siebers, Jeraj, & Mohan, 2000). The dose uncertainty in the target volume (PTV) for the final plan was calculated and appeared in the TPS console window after the second stage dose calculation.

There are a few other studies that have previously evaluated the overall effect of SU on dose calculation. But not about altering the per control point SU in IMRT plans. In 2000, Keall, Siebers, Jeraj, and Mohan (2000) found that the dose in Monte Carlo (MC) calculation does not significantly affect isodose lines and Dose Volume Histogram (DVH) for SU of 2% or lesser values. In 2004, Cheong, Suh, and Cho (2004) investigated the effect of SU on photon dose calculation using BEAMnrc and DOXXYZnrc MC simulation systems and evaluated SU based on DVH, isodose comparison, and root mean-square. In 2005, Ma et al. (2005) studied the issues related to the statistical analysis of MC dose calculations for realistic clinical beams using various variance reduction or time-saving techniques. Also, they discussed the effect of statistical uncertainties on dose prescription and monitor unit calculation for conventional treatment and IMRT based on MC simulations.

In 2016, Sarkar et al. (2016) investigated the interplay between Monte Carlo Variance (MCV) and Fluence Smoothing Factor (FSF) in VMAT for carcinoma of esophagus patients using a CMS-Monaco^{TM} Treatment Planning System (TPS). They reported that variation in FSF causes a difference in dosimetric and physical parameters for the treatment plan. In 2019, Palanisamy et al. (2019) explored the dosimetric impact of varying SU when calculating the dose of VMAT plans, and in 2021, Rembish et al. (2021) determined the severity of the effects on VMAT dose calculations caused by varying per control point SU in an MC-based TPS. Also, they assessed the impact of the uncertainty during DVH evaluation.

The goal of IMRT planning is to shape the radiation dose to avoid or reduce exposure of healthy tissue and limit the side effects of treatment while delivering a therapeutic dose to the cancer. According to the best of our knowledge, no precise data are available for the optimal acceptance level of SU% % per control point for different diagnoses in IMRT.

Also, no one studied the Dosimetric Impact on IMRT Plans of altering the per control point SU in Monaco TPS. Therefore, the purpose of this study is to evaluate the dosimetric impact on IMRT plans of altering the per control point SU (1% - 6%) using Elekta's Monaco TPS for three different diagnoses (Larynx, Esophagus, and Prostate).

METHODOLOGY

CT Simulation and Radiotherapy Treatment Machine

In this research work, three different diagnoses, which have high diversity, such as the Larynx, Oesophagus, and Prostate, were planned using the IMRT technique. A total of nine patients, three from each diagnosis, were selected for this study. The necessary CT image sets of all nine patients were obtained using a CT simulator (Siemens Healthineers, SOMATOM Confidence). The CT slice thickness of 5 mm was obtained for each clinical case for treatment planning. All generated IMRT plans were delivered using a 6 MV photon beam of Elekta Synergy Platform linear accelerator and its having a 1 cm multi-leaf collimator (MLC) at the iso-center.

Contouring and Dose Prescription

The tumor volume (Planning Target Volume - PTV) and Organs At Risk (OARs) volumes were contoured, and the doses prescribed to the Larynx, Oesophagus, and Prostate were 66 Gy/30 fractions, 50.4 Gy/28 fractions, and 78 Gy/39 fractions, respectively.

Treatment Planning System (TPS)

In this research work, the Monaco 5.11.02 TPS (IMPAC Medical System, Inc., Maryland Heights, MU, USA) was used to generate IMRT plans. It has a two-stage process of optimizing dose distribution. At the first stage, the ideal fluence distribution of a beam is optimized to meet a user-defined prescription for a single set of beams. At the second stage, the ideal distribution is transmitted into a set of segments where the shapes and weights are optimized based on the same prescription. For this research work, the Monte Carlo (MC) algorithm was used for dose calculation to generate an IMRT plan.

The Dosimetric Parameters used in Monaco TPS

All the 54 IMRT plans were generated using the dosimetric parameters, which are given in Table 1 below. By keeping these parameters constant, IMRT plans were generated using MC dose calculation algorithm only by varying per control point SU 1%, 2%, 3%, 4%, 5%, and 6%. To analyze IMRT plans, different dosimetry indices were used as mentioned below.

Table 1. The Dosimetric Parameters used in Monaco TPS

Parameter	Value
Delivery Mode	dMLC
CT Slice Thickness	0.5 cm
Grid Size	0.3 cm
Beamlet Width	0.3 cm
Control Points	40
Segment Width	0.5 cm
Auto Flash Margin	0.2 cm
Surface Margin	0.3 cm
Target Margin	0.8 cm
Fluence Smoothing	Medium

Dosimetric Indices used for IMRT Plan Evaluation

In this study, we used several dosimetric indices for IMRT Plan evaluation. Such as, Conformity Index (CI), Heterogeneity Index (HI), Target Dose and Critical Organ Doses, Dose Calculation Time (DCT), Treatment Delivery Results (IMRT Patient Specific QA and Gamma Indices), and Dose Volume Histogram (DVH).

- Conformity Index (CI)

The Conformity Index (CI) describes the degree to which the prescribed isodose volume conforms to the shape and size of the target volume. This value is only reported for Monaco plans (Elekta, 2017). The CI formula is given in equation 1:

$$CI = \frac{V_{Rx}^2}{(TV * V_{RI})} \quad (1)$$

where, TV = Structure Volume, V_{Rx} = is the structure volume covered by the Dose of Interest and V_{RI} is the total volume of the Dose of Interest.

- Heterogeneity Index (HI)

The Heterogeneity Index (HI) describes the uniformity of dose within a target volume and is directly calculated from the statistics of the DVH. This value is only reported for Monaco plans (Elekta, 2017). The HI formula is is given in equation 2:

$$HI = \frac{D_{5\%}}{D_{95\%}} \tag{2}$$

where, D_5% is the dose delivered to the hottest 5% of the tissue volume. D_{95}% is the minimum dose received by 95% of the tissue volume.

- Target Dose and Organ At Risk (OAR) Doses

The target dose (Dose to PTV) was analyzed as D95% (the dose received by 95% of the volume of PTV and V95% (the volume received 95% of the prescribed dose). Moreover, the maximum dose (Dmax) and mean dose (Dmean) for PTV and Organ at Risk (OAR) were analyzed for all three clinical cases. The OAR dose constraints (Table 2) were taken from the Practical Radiotherapy Planning book (5th Edition) (Morris, Roques, Ahmad, & Loo, 2023).

Table 2: Organ at Risk (OAR) Dose Constraints

Organ	Constraint	Optimal	Mandatory
Brainstem	Dmax whole organ		54 Gy (60 Gy if PRV used)
Spinal Cord	Dmax to PRV (cord +5 mm or spinal canal)		50 Gy (48 Gy if concomitant chemotherapy)
Parotid Gland	Mean Dose	24 Gy	
Lens	Dmax	10 Gy	
Heart	Mean Dose	25 Gy	30 Gy
Heart	V30 Gy	45 %	
Heart	V40	30 %	
Lungs	V20 Gy	35 % (25 % if risk factors)	
Lungs	Mean Dose	18 Gy	
Bladder	V50 Gy	50 %	
Bladder	V60 Gy	25 %	50 %
Femoral Heads	V50 Gy	5 %	50 %
Kidney (each)	V20 Gy	25 %	30 %
Kidney (both)	V20 Gy	30 %	35 %
Rectum	V30 Gy	70 %	80 %
Rectum	V40 Gy	51 %	65 %
Rectum	V50 Gy	38 %	50 %
Rectum	V60 Gy	27 %	35 %
Rectum	V70 Gy	15%	20 %

- Dose Calculation Time (DCT)

The dose calculation time was measured from the Monaco TPS optimization console window, which could give the dose calculation start and end time for all IMRT plans with different per control point SU values ranging from 1% to 6%. The total calculation time was defined as the time difference between the start and finish time of the MC dose calculation. For this research work, HP Z840 workstations, 128 GB RAM, Intel(R) Xeon(R) CPU E5-2697 v3 @ 2.60GHz (2 processors), and the 64-bit Operating system were used.

- Treatment Delivery Results (IMRT Patient Specific QA and Gamma Indices

The MatriXXEvolution (IBA) instrument and myQA software (Version 2019-002 (2.12.15.0), IBA Dosimetry GmbH, Germany) were used for the IMRT patient-specific QA with Elekta Synergy Platform Linear Accelerator. The MatriXX Evolution has 1020 air vented pixel ionization chambers arranged in a 32 x 32 grid (except for the four corner positions where chambers are missing) that cover an active field of 24.4 cm x 24.4 cm at 100 cm Source to Detector Distance (SDD). The distance between the individual chambers is 7.62 mm center to center. The diameter is 4.5
mm. Also, this MatriXXEvolution includes a temperature and pressure sensor to perform an automated k (t, p) correction of the chamber signal. The effective point of measurement is 3 mm below the MartiXXEvolution housing surface. The measured data is then transmitted to a PC or laptop via a standard Ethernet interface in the PC or laptop. The two-dimensional (2D) Gamma indices were compared at the isocenter between measured dose and TPS planned dose based on the dose to distance agreement (3%, 3mm) with 5% threshold value.

- Dose Volume Histogram

A Dose Volume Histogram (DVH) is a histogram that represents radiation dose (cGy or %) in the x-axis and volume (%) in the y-axis in radiation therapy planning. DVHs are most commonly used as a plan evaluation tool. Also, it is used to compare doses from different plans or to different structures. DVHs were introduced by Michael Goitein and Verhey in 1979 (Shipley et al., 1979). The ”volume” referred to in DVH analysis is a target of radiation treatment, a healthy organ near a target, or an arbitrary structure, and DVH summarizes 3D dose distributions in a graphical 2D format. In present radiation therapy, 3D dose distributions are typically created in a computerized TPS based on a 3D reconstruction of a CT scan.

STATISTICLE ANAYLISYS

The Statistical analysis was performed for all three diagnoses (for 54 IMRT Plans) using the percentage variation technique. Also, the comparison results were represented using tables, figures, and charts with the aid of OriginPro and overleaf softwares.

RESULTS & DISCUSSION

The dosimetric parameters were evaluated using the results of dosimetric indices. Some similarities and differences were observed due to the impact of Monte Carlo (MC) dose calculation uncertainty (per control point). The comparison results were analyzed using descriptive and inferential statistics. For the comparison process, we used several statistical terms in Monaco 5.11.02 Treatment Planning System (TPS), like mean dose, and max dose. The mean dose (cGy or Gy) is the averaged sampled dose within the total volume of the structure that is within the calculation volume, and the max dose (cGy or Gy) is the largest sampled dose within the total volume of the structure that is within the calculation volume (ICRU, 2010).

According to the measured average results shown in Table 3-5, the PTV dose coverage slightly changed as the per control point Statistical Uncertainty (SU) increased from 1% - 6% for PTV Dmean, PTV D95% (dose received by 95% volume of PTV), and V95% (the volume received 95% of the prescribed dose). This is primarily due to the **nature of the MC dose calculation algorithm** used in the Monaco Treatment Planning System. The MC algorithm simulates particle interactions to calculate dose. A **higher SU** allows **fewer particle histories** (simulations), which **speeds up the calculation** but introduces **greater stochastic noise**. With higher SU, random dose fluctuations can slightly raise or lower the average depending on spatial variation of statistical noise (**Miften et al., 2018).**

However, the maximum dose to PTV (PTV Dmax) increased as the per control point SU increased from 1% to 6% with a significant dose difference. This is a well-known and expected behavior of **MC-based dose calculation** systems. Unlike D95% or Dmean (which are averages), **Dmax is based on one or a few voxels**. When SU increases, **even a single voxel with a random high dose** due to low sampling is enough to **raise Dmax** significantly. This makes Dmax particularly **unstable** at high SU values (Low, Moran, Dempsey, Dong, & Oldham, 2011).

The Global Max of the plan slightly increased with per control point SU. This is also a characteristic effect of **MC dose calculation noise.** The **Global Maximum Dose** is usually defined as the **dose in the single highest-dose voxel** in the entire 3D dose matrix. With higher SU, **random fluctuations** (positive outliers) in individual voxels are more likely. Therefore, one or a few voxels may report **artificially high dose values**, raising the Global Max (Low, Moran, Dempsey, Dong, & Oldham, 2011).

According to the measured average results given in Table 3, the mean dose to Organs at Risk (OARs) such as the left parotid and right parotid showed a small variation. The max dose to brain stem, spinal cord, left lens, and right lens also showed small dose differences. But no clinically and statistically significant dose differences were observed.

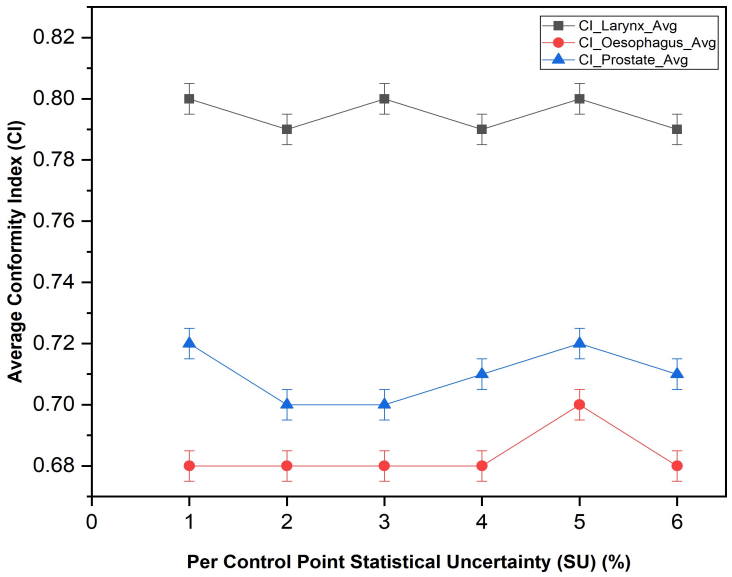

Figure 1. Average Conformity Index (CI) Vs. Per Control Point Statistical Uncertainty (SU) (%)

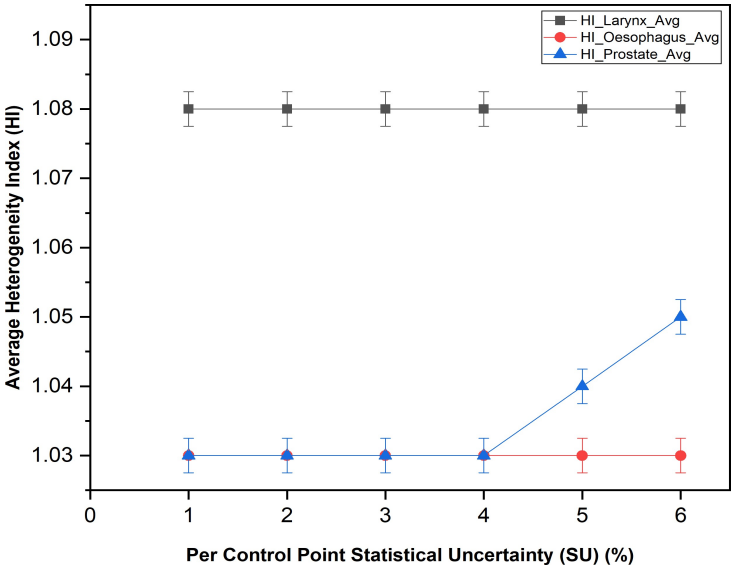

Figure 2. Average Heterogeneity Index (HI) Vs. Per Control Point Statistical Uncertainty (SU) (%)

According to the measured average results given in Table 4, the mean dose to OARs such as the heart, left lung and right lung, left kidney, and right kidney showed a small difference. The max dose to spinal code also showed a small dose difference. But no clinically and statistically significant dose differences were observed. According to the measured results given in Table 5, the mean dose to OARs such as the rectum, bladder, left pelvic bone, and right pelvic bone showed a small difference. But no clinically and statistically significant dose differences were observed.

According to the measured average results shown in Figure 1, no significant variation was observed between the Conformity Index (CI) values with per control point SU for Larynx, Oesophagus, and Prostate. A CI value of 1 indicates perfect conformity, but in clinical practice, values between 0.7 and 0.9 are considered acceptable, depending on the complexity of the case and treatment site (Feuvret et al., 2006).

There is a significant variation observed between Heterogeneity Index (HI) values with per control point SU for Prostate (Figure 2). This observation in **Monaco TPS** is indeed supported by studies focused on the **Monte Carlo-based dose calculation** used in Monaco. This behavior is particularly evident in **prostate IMRT/VMAT plans,** where the precision of dose gradients is affected by SU levels**.** The **higher per control point SU values can cause statistical noise,** leading to elevated **D5%** and suppressed **D95%** values—hence increasing the **HI** (Elekta AB, 2017).

According to the measured average results shown in Table 3-5, the gamma index (pass rate) (Miften et al., 2018), (Low et al., 2011) results showed a good pass rate of 97.5 % - 98.8 % for 3%, 3 mm dose to distance agreement with 5% threshold value for the per control point SU from 1% to 6% and no significant variation was observed by the influence of the per control point SU.

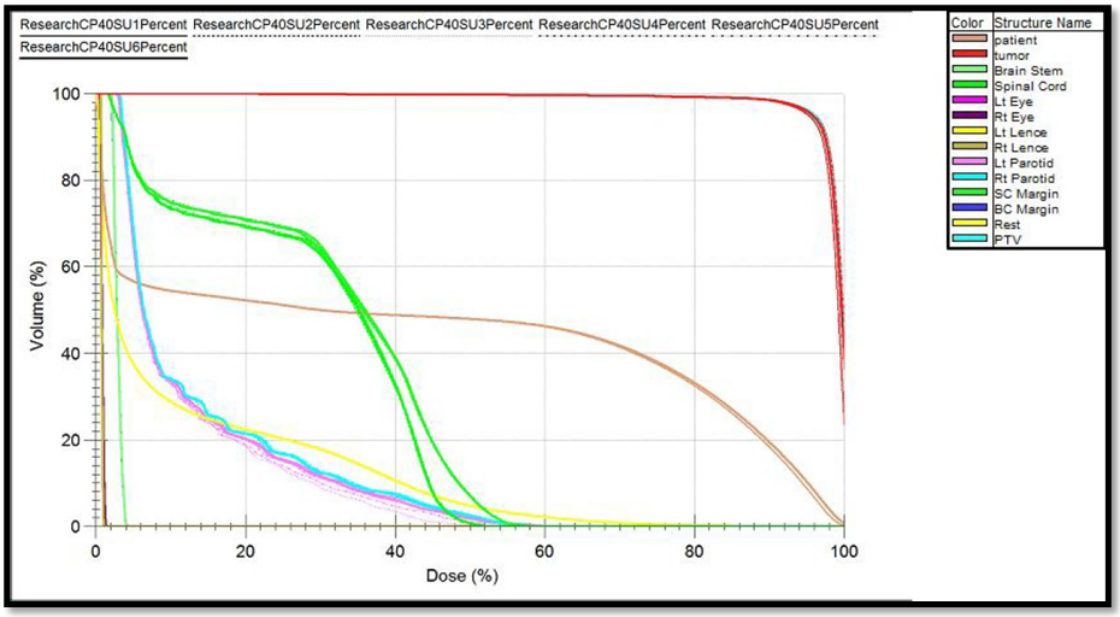

Figure 3. Average Dose Volume Histogram for Larynx

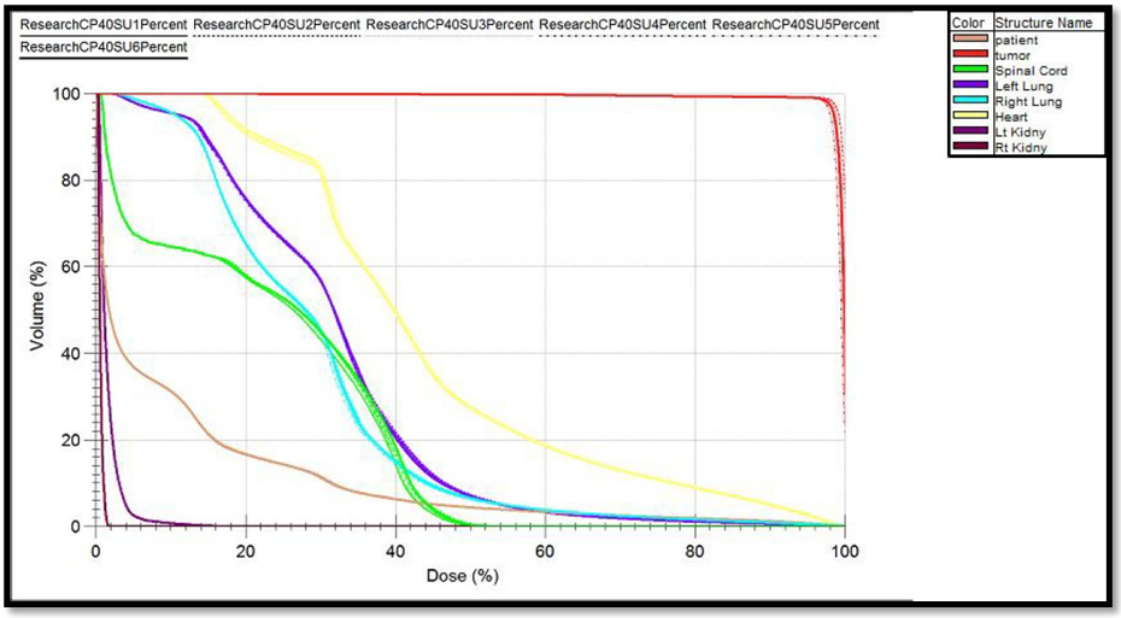

Figure 4. Average Dose Volume Histogram for Oesophagus

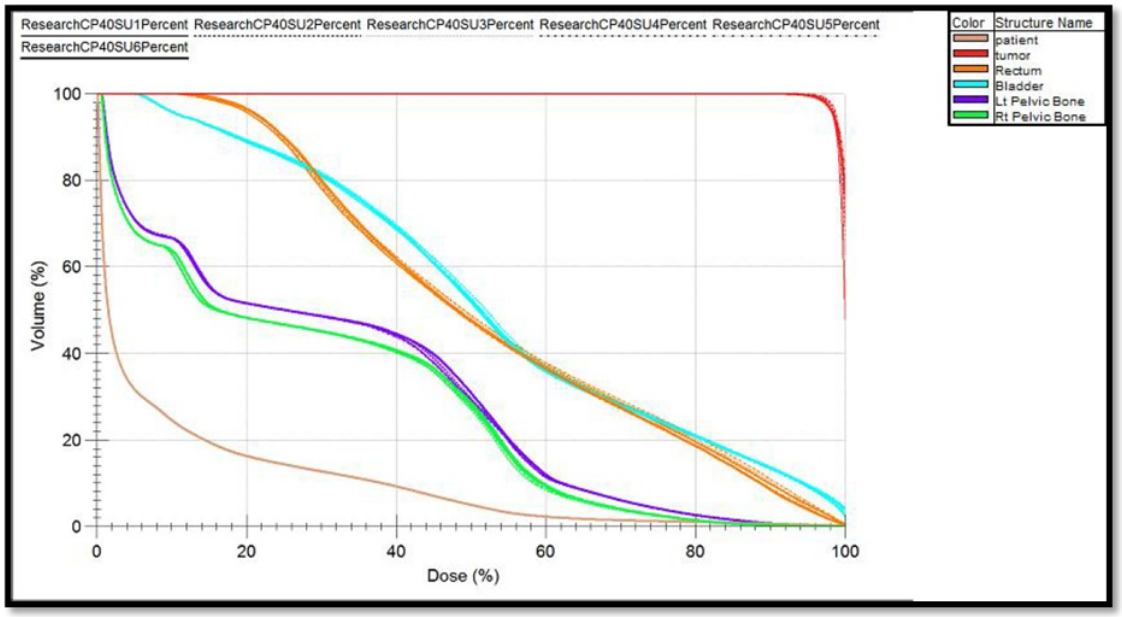

Figure 5. Average Dose Volume Histogram for Prostate

Figures 3-5 show the average Dose Volume Histogram (DVH) for Larynx, Oesophagus, and Prostate, respectively, for six different per control point SUs (Such as 1%, 2%, 3%, 4%, 5%, 6%). The measured average DVH results showed a very small dose difference between the per control point SU 1% - 6% and no significant dose differences were observed. According to the measured average results shown in Figure 6, there is an exponential relationship between dose calculation time and the per control point SU. The increase of per control point SU leads to a decrease in MC dose calculation time with a significant difference. Approximately reducing the per control point SU by a factor of two requires a four times increase in Central Processing Unit (CPU) time (Palanisamy, David, Durai, Bhalla, & Puri, 2019). Figure 7 indicates a linear relationship between average final dose uncertainty and the per control point SU values from 1% to 6%. The important fact is that the final dose uncertainty should be approximately 1% for the entire plan, and it shouldn't be greater than 1% for the entire plan (Elekta AB, 2017).

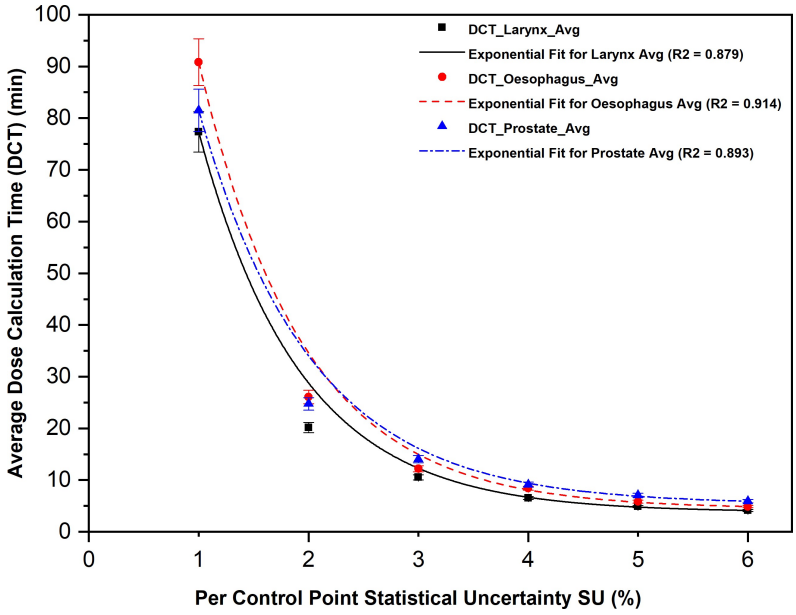

Figure 6. Average Dose Calculation Time (DCT) (min) Vs. Per Control Point Statistical Uncertainty (SU) (%)

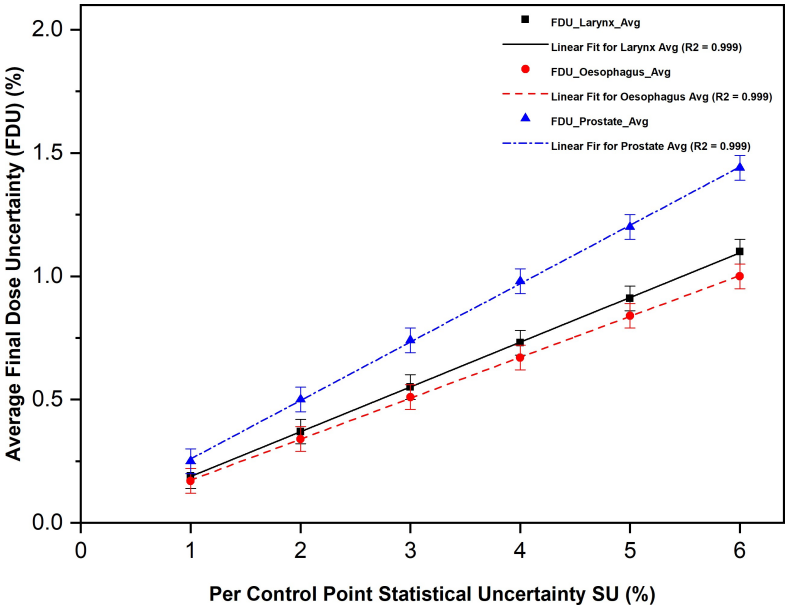

Figure 7: Average Final Dose Uncertainty (%) Vs. Per Control Point Statistical Uncertainty (SU) (%)

Table 3: Average Comparison Results of Dosimetric Indices for Different Per Control Point Statistical Uncertainty (SU) Levels for Larynx

Target and OARs Larynx	SU 1%	SU_2%	SU_3%	SU_4%	SU_5%	SU_6%
PTV 66 D95% (cGy)	6208.60 ±11.60	6238.73 ±23.11	6209.03 ±33.96	6219.47 ±45.65	6213.13 ±56.78	6224.47 ±68.31
PTV 66 Dmax (cGy)	6908.70 ±12.90	6924.47 ±25.63	6925.10 ±37.86	6932.83 ±50.85	6961.60 ±63.59	6982.30 ±76.58
PTV 66 Dmean (cGy)	6487.07 ±12.12	6511.67 ±24.11	6490.13 ±35.48	6501.53 ±47.69	6496.07 ±59.35	6512.03 ±71.43
PTV 66 V95% (%)	93.81 ±0.19	94.38 ±0.37	93.73 ±0.55	93.78 ±0.73	93.78 ±0.91	94.16 ±1.10
PTV 66 Heterogeneity Index	1.08 ±0.002	1.08 ±0.004	1.08 ±0.006	1.08 ±0.008	1.08 ±0.009	1.08 ±0.012
PTV 66 Conformity Index	0.80 ±0.001	0.79 ±0.003	0.80 ±0.004	0.79 ±0.006	0.80 ±0.007	0.79 ±0.009
Brain Stem Dmax (cGy)	1072.60 ±2.68	1202.47 ±6.08	1152.77 ±8.75	1136.80 ±11.36	1102.43 ±13.59	1164.63 ±17.52
Spinal Cord Dmax (cGy)	3680.90 ±6.89	3679.20 ±13.66	3678.57 ±20.14	3687.30 ±27.08	3712.33 ±33.93	3676.87 ±40.34
Lt Parotid Dmean (cGy)	1841.53 ±3.66	1794.90 ±7.13	1785.67 ±10.54	1819.60 ±14.29	1797.97 ±17.57	1792.87 ±20.91
Rt Parotid Dmean (cGy)	1775.77 ±3.50	1836.20 ±7.27	1824.23 ±10.63	1810.53 ±14.14	1790.10 ±17.29	1784.20 ±20.72
Lt Lens Dmax (cGy)	60.77 ±0.12	62.33 ±0.23	61.77 ±0.35	63.83 ±0.48	61.17 ±0.57	64.07 ±0.72
Rt Lens Dmax (cGy)	61.53 ±0.12	62.30 ±0.24	61.63 ±0.35	63.17 ±0.47	61.87 ±0.58	64.10 ±0.72
Global Max of the Plan (%)	104.68 ±0.19	104.92 ±0.37	104.92 ±0.55	105.11 ±0.73	105.48 ±0.91	105.96 ±1.10
Dose Calculation Time (mins)	77.32 ±3.91	20.14 ±1.02	10.54 ±0.53	6.55 ±0.33	4.90 ±0.25	4.14 ±0.22
Gamma Pass Rate 3%, 3 mm	98.1 ±2.94	98.5 ±2.95	98.3 ±2.95	98.6 ±2.96	98.4 ±2.95	98.8 ±2.96

Table 4. Average Comparison Results of Dosimetric Indices for Different Per Control Point Statistical Uncertainty (SU) Levels for Oesophagus

Target and OARs Larynx	SU 1%	SU_2%	SU_3%	SU_4%	SU_5%	SU_6%
PTV 50.4 D95% (cGy)	4950.47 ± 8.43	4963.87 ± 16.73	4952.93 ± 25.12	4955.83 ± 33.41	4939.50 ± 38.88	4949.03 ± 49.71
PTV 50.4 Dmax (cGy)	5189.47 ± 8.83	5209.37 ± 17.56	5210.03 ± 26.44	5212.10 ± 35.14	5226.63 ± 44.16	5261.10 ± 52.85
PTV 50.4 Dmean (cGy)	4997.70 ± 8.50	5013.07 ± 16.90	5002.13 ± 25.37	5010.37 ± 33.79	4999.80 ± 42.23	5011.73 ± 50.34
PTV 50.4 V95%	98.67 ± 0.17	98.71 ± 0.34	98.68 ± 0.51	98.73 ± 0.67	98.70 ± 0.84	98.71 ± 1.00
PTV 50.4 Heterogeneity Index	1.03 ± 0.002	1.03 ± 0.004	1.03 ± 0.005	1.03 ± 0.007	1.03 ± 0.009	1.03 ± 0.010
PTV 50.4 Conformity Index	0.68 ± 0.001	0.68 ± 0.002	0.68 ± 0.003	0.68 ± 0.005	0.70 ± 0.006	0.68 ± 0.007
Heart Dmean (cGy)	2303.07 ± 3.93	2278.23 ± 7.70	2285.87 ± 11.64	2276.40 ± 15.38	2273.73 ± 19.26	2290.83 ± 23.09
Spinal Cord Dmax (cGy)	3560.20 ± 6.23	3584.77 ± 12.43	3576.33 ± 18.70	3558.87 ± 24.73	3572.70 ± 31.15	3547.00 ± 36.66
Rt Lung Dmean (cGy)	1523.03 ± 2.61	1516.70 ± 5.11	1522.23 ± 7.74	1522.50 ± 10.28	1511.73 ± 12.79	1518.63 ± 15.28
Lt Lung Dmean (cGy)	1458.57 ± 2.49	1456.60 ± 4.92	1455.77 ± 740	1455.80 ± 9.83	1448.57 ± 12.26	1456.53 ± 14.65
Lt Kidney Dmean (cGy)	168.80 ± 0.38	167.77 ± 0.78	164.23 ± 1.12	162.93 ± 1.50	165.97 ± 1.91	162.77 ± 2.22
Rt Kidney Dmean (cGy)	40.70 ± 0.07	40.73 ± 0.15	40.80 ± 0.22	40.67 ± 0.29	40.57 ± 0.36	40.60 ± 0.43
Global Max of the Plan (%)	102.97 ± 0.17	103.36 ± 0.34	103.38 ± 0.51	103.42 ± 0.67	103.70 ± 0.84	104.39 ± 1.00
Dose Calculation Time (mins)	90.8 ± 4.66	26.06 ± 1.32	12.18 ± 0.62	8.42 ± 0.43	5.85 ± 0.30	4.89 ± 0.25
Gamma Pass Rate 3%, 3 mm	97.5 ± 2.93	98.3 ± 2.95	97.9 ± 2.94	98.1 ± 2.94	97.7 ± 2.93	98.4 ± 2.95

Table 5. Average Comparison Results of Dosimetric Indices for Different Per Control Point Statistical Uncertainty (SU) Levels for Prostate

Target and OARs_Larynx	**SU_1%**	**SU_2%**	**SU_3%**	**SU_4%**	**SU_5%**	**SU _6%**
PTV 78 D95% (cGy)	7657.57 ± 18.89	7672.97 ± 38.12	7681.73 ± 56.61	7662.20 ± 75.37	7633.23 ± 91.90	7615.20 ± 109.41
PTV 78 Dmax (cGy)	8046.73 ± 19.85	8075.70 ± 40.12	8118.27 ± 59.83	8139.67 ± 80.06	8132.50 ± 97.93	8202.93 ± 117.88
PTV 78 Dmean (cGy)	7793.60 ± 19.23	7811.20 ± 38.80	7822.13 ± 57.65	7810.90 ± 76.83	7813.40 ± 94.07	7827.07 ± 112.47
PTV 78 V95% (cm3)	99.43 ± 0.2	99.54 ± 0.50	99.53 ± 0.74	99.39 ± 0.98	99 ± 1.20	98.77 ± 1.44
PTV 78 Heterogeneity Index	1.03 ± 0.003	1.03 ± 0.005	1.03 ± 0.008	1.03 ± 0.010	1.04 ± 0.012	1.05 ± 0.014
PTV 78 Conformity Index	0.72 ± 0.002	0.70 ± 0.004	0.70 ± 0.005	0.71 ± 0.007	0.72 ± 0.009	0.71 ± 0.011
Rectum Dmean (cGy)	4109.13 ± 9.89	4164.23 ± 20.69	4144.10 ± 30.53	4132.20 ± 40.63	4098.40 ± 49.35	4083.50 ± 58.68
Bladder Dmean (cGy)	3778.87 ± 9.40	3811.00 ± 19.09	3801.77 ± 28.27	3768.13 ± 37.42	3741.43 ± 45.53	3741.30 ± 54.08
Lt Pelvic Bone Dmean (cGy)	2168.93 ± 5.39	2180.77 ± 10.92	2170.37 ± 16.11	2159.70 ± 21.40	2181.27 ± 26.47	2193.07 ± 31.65
Rt Pelvic Bone Dmean (cGy)	2189.97 ± 5.46	2189.70 ± 11.02	2199.67 ± 16.41	2187.13 ± 21.80	2200.87 ± 26.84	2223.80 ± 32.26
Global Max of the Plan (%)	103.21 ± 0.25	103.73 ± 0.50	104.08 ± 0.74	104.45 ± 0.98	104.37 ± 1.20	105.16 ± 1.44
Dose Calculation Time (mins)	81.5 ± 4.11	24.74 ± 1.24	14.03 ± 0.71	9.12 ± 0.47	7.06 ± 0.36	5.92 ± 0.30
Gamma Pass Rate 3%, 3 mm	97.1 ± 2.91	97.7 ± 2.93	97.5 ± 2.93	97.6 ± 2.93	97.2 ± 2.92	97.6 ± 2.93

DISCUSSION

The Monte Carlo (MC) methods are mainly used in three distinct problem classes: optimization, numerical integration, and generating draws from a probability distribution. In Monaco 5.11.02 TPS, MC was used for optimization, and the MC method has been identified as the gold standard for dose calculation (Clements, Schupp, Tattersall, Brown, & Larson, 2018). At present, MC simulation calculates the dose very closely to reality, taking into account the contribution of secondary photons and electrons scattering and dose absorption, especially in homogeneous environments (Tugrul, 2021). The per control point SU is the percentage (%) SU per voxel, on a per-segment basis, that is willing to accept for the final dose calculation. So, the mean, per voxel, uncertainty in a central region of the dose of a segment is equal to the user-specified SU at the end of the dose calculation. A voxel is a measurement of volume in a structure that is to be imaged. Each voxel represents a defined volume and can be localized by coordinates on a three-dimensional (3D) grid. Here, the very important fact is that the smaller the per control point SU, the longer the dose calculation time. Also, when we used per control point SU values between 0.1% - 10%, the results should be a final dose uncertainty of approximately 1% for the plan in the central region of the target volume.

The main difference between Per Calculation SU and Per Control Point SU is based on the number of histories (Uyar & Günekbay, 2023) and the voxel. In other words, Per Calculation SU is fast because it estimates the number of histories for the entire plan (recommended value 1%). Per control Point SU gives better resolution because it uses percentage uncertainty per voxel on a per-segment basis. So it should vary for the number of control points. In this work, we used 40 control points to generate each IMRT plan. The MC dose calculation without any SU is the most worthwhile in an IMRT plan from the accuracy point of view. However, it would take infinite time to calculate. So the planner should accept a certain range for this calculation uncertainty. The SU of MC is inversely proportional to the volume of the dose voxel (Mohan, Antolak, & Hendee, 2001). For example, when decreasing the voxel size from 5 mm to 3 mm, it caused to increase in the Monte Carlo calculation time of approximately fivefold. Also, when reducing the SU by a factor of two, it caused the MC calculation time to be fourfold (Figure 6). So it was very crucial in decreasing/ increasing voxel size or SU in both ways.

Overall analysis of this study suggests that there were no diagnosis-specific dosimetric variations. As reported by Jiang et al. (Jiang, Pawlicki, & Ma, 2000), large Statistical Uncertainties (SUs) are expected to blur the Dose Volume Histogram (DVH) curves and may become unreliable. The statistical noise should have practically no effect on inverse treatment planning (as IMRT) because the intensity along a ray is affected by the average of dose values over a large number of voxels lying along the ray and not by the dose in any one voxel (Mohan, Antolak, & Hendee, 2001).

It was suggested that large SU can be used for large tumors and OARs such as parallel organs (Palanisamy, David, Durai, Bhalla, & Puri, 2019). The effect of the per control point SU in this study showed no significant dose differences on the mean dose to the target and OAR volumes. So, it is suggested that SU can be used up to 5% for parallel organs. For the structures with small volumes (such as small tumors, lens), Monaco does not recommend using per control point SU higher than 5%. If we use a higher value (higher than 5%), it causes the system to underestimate the cost function value assigned to that structure (Elekta, 2017).

Significant variation was observed in average dose calculation time and the per control point SU. There is an exponential relationship observed between average dose

calculation time and the per control point SU (Figure 6). The dose calculation time may not be too long. Also, the gamma index showed a good pass rate for all three different diagnoses (such as Larynx, Oesophagus, and Prostate), and there are no significant variations were observed in the gamma pass rate for all three diagnoses. The final dose uncertainty should be approximately 1% for the entire plan (Elekta, 2017), and it shouldn't be greater than 1% for the entire plan (Figure 7).

Finally, based on all the measured average results, as well as considering other important factors and constraints, we recommend maintaining a control point SU value of 3% without compromising the quality or delivery of the plan. Additionally, we analyzed the percentage variations concerning the 3% per control point SU for the Larynx, Oesophagus, and Prostate (refer to Tables 6-8).

Table 6. Percentage Variation values with respect to 3% for Larynx

Target and OARs___Larynx (wrt.3%)	SU_1%	SU_2%	SU_4%	SU_5%	SU_6%
PTV_66_D95% (cGy)	0.01	0.48	0.17	0.07	0.25
PTV_66_Dmax (cGy)	0.24	0.01	0.11	0.53	0.83
PTV 66 Dmean (cGy)	0.05	0.33	0.18	0.09	0.34
PTV_66_V95% (%)	0.09	0.69	0.05	0.05	0.46
PTV 66 Heterogeneity Index	0	0	0	0	0
PTV_66_Conformity Index	0	1.25	1.25	0	1.25
Brain Stem_Dmax (cGy)	6.95	4.31	1.39	4.37	1.03
Spinal Cord_Dmax (cGy)	0.06	0.02	0.24	0.92	0.05
Lt Parotid_Dmean (cGy)	3.13	0.52	1.9	0.69	0.4
Rt Parotid_Dmean (cGy)	2.66	0.66	0.75	1.87	2.19
Lt Lens_Dmax (cGy)	1.62	0.91	3.33	0.97	3.72
Rt Lens_Dmax (cGy)	0.16	1.09	2.5	0.39	4.01
Global Max of the Plan (%)	0.23	0	0.18	0.53	0.99
Gamma Pass Rate_3%, 3 mm	0.20	0.20	0.31	0.10	0.51

Table 7: Percentage Variation values with respect to 3% for Oesophagus

Target and OARs Oesophagus (wrt.3%)	SU_1%	SU_2%	SU_4%	SU_5%	SU_6%
PTV 50.4 D95% (cGy)	0.05	0.22	0.06	0.27	0.08
PTV 50.4 Dmax (cGy)	0.39	0.01	0.04	0.32	0.98
PTV 50.4 Dmean (cGy)	0.09	0.22	0.16	0.05	0.19
PTV 50.4 V95%	0.01	0.03	0.05	0.02	0.03
PTV 50.4 Heterogeneity Index	0.00	0.00	0.00	0.00	0.00
PTV 50.4 Conformity Index	0.00	0.00	0.00	2.94	0.00
Heart Dmean (cGy)	0.75	0.33	0.41	0.53	0.22
Spinal Cord Dmax (cGy)	0.45	0.24	0.49	0.10	0.82
Rt Lung Dmean (cGy)	0.05	0.36	0.02	0.69	0.24
Lt Lung Dmean (cGy)	0.19	0.06	0.00	0.49	0.05
Lt Kidney Dmean (cGy)	2.78	2.16	0.79	1.06	0.89
Rt Kidney Dmean (cGy)	0.25	0.17	0.32	0.56	0.49
Global Max of the Plan (%)	0.40	0.02	0.04	0.31	0.98
Gamma Pass Rate 3%, 3 mm	0.41	0.41	0.20	0.20	0.51

Table 8. Percentage Variation values with respect to 3% for Prostate

Target and OARs Prostate (wrt.3%)	SU_1%	SU_2%	SU_4%	SU_5%	SU_6%
PTV 78 D95% (cGy)	0.31	0.11	0.25	0.63	0.87
PTV 78 Dmax (cGy)	0.88	0.52	0.26	0.18	1.04
PTV 78 Dmean (cGy)	0.36	0.14	0.14	0.11	0.06
PTV 78 V95% (cm3)	0.1	0.01	0.14	0.53	0.76
PTV 78 Heterogeneity Index	0	0	0	0.97	1.94
PTV 78 Conformity Index	2.86	0	1.43	2.86	1.43
Rectum Dmean (cGy)	0.84	0.49	0.29	1.1	1.46
Bladder Dmean (cGy)	0.6	0.24	0.88	1.59	1.59
Lt Pelvic Bone Dmean (cGy)	0.07	0.48	0.49	0.5	1.05
Rt Pelvic Bone Dmean (cGy)	0.44	0.45	0.57	0.05	1.1
Global Max of the Plan (%)	0.84	0.34	0.36	0.28	1.04
Gamma Pass Rate 3%, 3 mm	0.41	0.21	0.10	0.31	0.10

According to the calculated percentage variation values (Table 6-8) with respect to a 3% per control point SU, showed no any significant variation between the dosimetric indices and the per control point SU (%) values for all three diagnoses (Larynx, Oesophagus, and Prostate).

CONCLUTION

This study proposed an optimal acceptable range for the per Control Point Statistical Uncertainty (SU) in Monte Carlo Dose calculations during IMRT planning in Monaco 5.11.02 Treatment Planning System (TPS). Based on the measured average results, a 3% per control point SU is acceptable for all three diagnoses (Larynx, Oesophagus, and Prostate) in IMRT planning, allowing for reduced calculation time without compromising target coverage, Organ at Risk (OAR) doses, or plan delivery.

Conflict of Interest

None declared.

Financial Disclosure

The authors did not receive any kind of grant or financial support from any organization for the present study.

REFERENCES

[1] **Bortfeld, T.** (2006). IMRT: A review and preview. *Physics in Medicine and Biology, 51*(13), R363–R379. https://doi.org/10.1088/0031-9155/51/13/R21

[2] Carol, M. P. (1995). Peacock: A system for planning and rotational delivery of intensity-modulated fields. *International Journal of Imaging Systems and Technology, 6*(1), 56–61. Webb, S., 2001. Intensity-modulated radiation therapy (IMRT): a clinical reality or a technical exercise? *British Journal of Radiology*, 74(881), pp.593–594.

[3] Cheong, K. H., Suh, T. S., & Cho, B. C. (2004). The effects of the statistical uncertainties in Monte Carlo photon dose calculation for radiation therapy. *Journal of Radiation Protection and Research, 29*(2), 105–115.

[4] Chetty, I. J., Curran, B., Cygler, J. E., DeMarco, J. J., Ezzell, G., Faddegon, B. A., … Seuntjens, J. (2007). Report of the AAPM Task Group No. 105: Issues associated with clinical implementation of Monte Carlo–based photon and electron external beam treatment planning. *Medical Physics, 34*(12), 4818–4853. https://doi.org/10.1118/1.2804935

[5] **Clements, M., Schupp, N., Tattersall, M., Brown, A., & Larson, R. (2018).** Monaco treatment planning system tools and optimization processes. *Medical Dosimetry, 43*(2), 106–117. https://doi.org/10.1016/j.meddos.2017.12.002

[6] **Delaney, G., Jacob, S., Featherstone, C., & Barton, M. (2005).** The role of radiotherapy in cancer treatment: Estimating optimal utilization from a review of evidence-based clinical guidelines. *Cancer, 104*(6), 1129–1137. https://doi.org/10.1002/cncr.21324

[7] Elekta AB. (2017). Monaco 5.11 Reference Guide – Physics Module. Stockholm, Sweden: Elekta AB.

[8] Feuvret, L., Noël, G., Mazeron, J. J., & Bey, P. (2006). Conformity index: A review. *International Journal of Radiation Oncology, Biology, Physics*, 64(2), 333–342. https://doi.org/10.1016/j.ijrobp.2005.09.028

[9] Goodall, S. K., & Ebert, M. A. (2020). Recommended dose voxel size and statistical uncertainty parameters for precision of Monte Carlo dose calculation in stereotactic radiotherapy: Investigation using Monaco 5.11.02. *Journal of Applied Clinical Medical Physics, 21*(12), 120–130. https://doi.org/10.1002/acm2.13077

[10] **Gupta, T., Agarwal, J. P., Ghosh-Laskar, S., & Shrivastava, S. K.** (2009). A prospective comparative study of time requirements and resource burden for intensity modulated radiotherapy versus 3-dimensional conformal radiotherapy in head and neck cancer. *Journal of Cancer Research and Therapeutics, 5*(2), 126–131.

[11] Hall, E. J., & Giaccia, A. J. (2019). *Radiobiology for the radiologist* (8th ed.). Philadelphia, PA: Wolters Kluwer.

[12] **Intensity Modulated Radiation Therapy Collaborative Working Group.** (2001). Intensity-modulated radiation therapy: Emerging cancer treatment technology. *British Journal of Cancer, 92*(10), 1819–1824. https://doi.org/10.1038/sj.bjc.6602589

[13] **International Commission on Radiation Units and Measurements (ICRU). (2010).** *Prescribing, Recording, and Reporting Photon-Beam Intensity-Modulated Radiation Therapy (IMRT).* **ICRU Report 83.** Journal of the ICRU, **10**(1), 1–106. https://doi.org/10.1093/jicru/ndq00

[14] **Jiang, S. B., Pawlicki, T., & Ma, C.-M. (2000).** Removing the effect of statistical uncertainty on dose-volume histograms from Monte Carlo dose calculations. *Physics in Medicine & Biology, 45*(8), 2151–2161. https://doi.org/10.1088/0031-9155/45/8/312

[15] Keall, P., Siebers, J., Jeraj, R., & Mohan, R. (2000). The effect of dose calculation uncertainty on the evaluation of radiotherapy plans. *Medical Physics, 27*(3), 478–484. https://doi.org/10.1118/1.598909

[16] **Khan, F. M., & Gibbons, J. P. (2014).** *The physics of radiation therapy* (5th ed.). Lippincott Williams & Wilkins

[17] Kry, S. F., *et al.* (2019). Dosimetric impact of statistical uncertainty on Monte Carlo dose calculation in VMAT plans. *Medical Physics*, **46**(3), 1225–1233.

[18] Lawrence, T. S., & Cox, J. D. (1995). Intensity-modulated radiation therapy: Clinical applications and early experience. *International Journal of Radiation Oncology, Biology, Physics*, *31*(4), 955–962.

[19] LoSasso, T., Chui, C. S., & Ling, C. C. (1998). Physical and dosimetric aspects of a multileaf collimation system used in the dynamic mode for implementing intensity modulated radiotherapy. *Medical Physics, 25*(10), 1919–1927.

[20] Low, D. A., Moran, J. M., Dempsey, J. F., Dong, L., & Oldham, M. (2011). Dosimetry tools and techniques for IMRT. *Medical Physics, 38*(3), 1313–1338.

[21] Ma, C., Li, J., Jiang, S., Pawlicki, T., Xiong, W., Qin, L., et al. (2005). Effect of statistical uncertainties on Monte Carlo treatment planning. *Physics in Medicine & Biology, 50*(5), 891–907. https://doi.org/10.1088/0031-9155/50/5/001

[22] Miften, M., Olch, A., Mihailidis, D., Moran, J., Pawlicki, T., Molineu, A., et al. (2018). Tolerance limits and methodologies for IMRT measurement-based verification QA: Recommendations of AAPM Task Group No. 218. *Medical Physics, 45*(4), e53–e83.

[23] **Mohan, R., Antolak, J., & Hendee, W. R. (2001).** Monte Carlo techniques should replace analytical methods for estimating dose distributions in radiotherapy treatment planning. *Medical Physics, 28*(2), 123–126. https://doi.org/10.1118/1.1339879

[24] **Mohan, R.** (2005). Intensity-modulated radiation therapy: What is it, why it is done, and how it is done. *Cancer Journal, 11*(5), 317–324.

[25] Morris, S., Roques, T., Ahmad, S., & Loo, S. (2023). *Practical radiotherapy planning*. CRC Press.

[26] **Palta, J. R., & Mackie, T. R. (2011).** *Teletherapy: Present and future*. Medical Physics Publishing.

[27] Palanisamy, M., David, K., Durai, M., Bhalla, N., & Puri, A. (2019). Dosimetric impact of statistical uncertainty on Monte Carlo dose calculation algorithm in volumetric modulated arc therapy using Monaco TPS for three different clinical cases. *Reports of Practical Oncology and Radiotherapy, 24*(2), 188–199. https://doi.org/10.1016/j.rpor.2018.10.006

[28] Papiez, L., & Langer, M. (2006). Monte Carlo dose calculations in radiation therapy: A review. *Reports of Practical Oncology and Radiotherapy, 11*(5), 245–253. https://doi.org/10.1016/S1507-1367(06)70955-5

[29] **Podgorsak, E. B. (2005).** *Radiation oncology physics: A handbook for teachers and students*. International Atomic Energy Agency.

[30] Rembish, J., Myers, P., Saenz, D., Kirby, N., Papanikolaou, N., & Stathakis, S. (2021). Effects of varying statistical uncertainty using a Monte Carlo based treatment planning system for VMAT. *Journal of BUON, 26*(4), 1663–1668.

[31] Sarkar, B., Manikandan, A., Nandy, M., Munshi, A., Sayan, P., & Sujatha, N. (2016). Influence of Monte Carlo variance with fluence smoothing in VMAT treatment planning with Monaco TPS. *Indian Journal of Cancer, 53*(1), 158–161.

[32] Shipley, W. U., Tepper, J. E., Prout, G. R., Verhey, L. J., Mendiondo, O. A., Goitein, M., et al. (1979). Proton radiation as boost therapy for localized prostatic carcinoma. *JAMA, 241*(18),1912–19

[33] Taleei, R., & Tabrizi, P. R. (2019). Optimization of statistical uncertainty and calculation time in Monte Carlo dose calculation for radiotherapy treatment planning. *Journal of Applied Clinical Medical Physics, 20*(11), 153–160. https://doi.org/10.1002/acm2.12730

[34] **Tugrul, T. (2021).** Comparison of Monaco treatment planning system algorithms and Monte Carlo simulation for small fields in anthropomorphic RANDO phantom: The esophagus case. *Journal of Cancer Research and Therapeutics, 17*(6), 1370–1375. https://doi.org/10.4103/jcrt.JCRT_1562_20

[35] **Uyar, E., & Günekbay, Z. A. (2023).** Comparison of the number of history in Monte Carlo simulation programs. *arXiv*. https://arxiv.org/abs/2301.05916

[36] Vassiliev, O. N., Wareing, T. A., McGhee, J., Failla, G., Salehpour, M., & Mourtada, F. (2010). Validation of a new grid-based Boltzmann equation solver for dose calculation in radiotherapy with photon beams. *Physics in Medicine & Biology, 55*(3), 581–598. https://doi.org/10.1088/0031-9155/55/3/003

[37] Zhang, M., Moiseenko, V., Liu, M., Yan, D., & Fraass, B. A. (2007). Dose calculation accuracy in IMRT: Impacts on patient-specific QA and treatment. *Medical Physics, 34*(5), 1807–1814.

Development of a Solar-Powered, Automated Water Ionizer Using Graphite-Based Electrodes for Alkaline and Acidic Water Production

A.M.K.L Abeykoon[1*], M.D.Y Milani[1], H.M. B. I. Gunathilaka[1],R. C. W. Arachchige[1], D.M.K Muthumala[2]

[1]Materials Technology Section of Industrial Technology Institute, No. 363, Bauddhaloka Mawatha, Colombo 07, Sri Lanka
[2] Faculty of Technology, Wayamba University of Sri Lanka, Kuliyapitiya, Sri Lanka.

ABSTRACT

This study presents the development and automation of a novel water ionizer, designed to produce ionized water with precisely controlled pH levels through an advanced electrolysis process. The primary objective is to generate both alkaline and acidic water for various applications, including sterilization, cleaning, and drinking. With the increasing demand for alkaline water due to its potential human health benefits in reducing oxidative stress caused by free radicals, this research introduces a cost-effective, eco-friendly system that integrates innovative graphite-based electrode materials, automated control mechanisms, and a PV solar power system. These electrodes contribute to cost reduction, while the automation system enables precise regulation of pH levels, significantly enhancing the reliability and user convenience of the ionizer. Additionally, the system is powered by a solar cell setup, optimizing the use of renewable energy and aligning with sustainability goals by reducing dependence on conventional power sources.

Keywords: Water Ionizer, Graphite-Based Electrodes, Electrolysis Automation

lahiru@iti.lk*

INTRODUCTION

Water ionization technology has gained significant attention in recent years due to the increasing demand for alkaline water, which is valued for its potential health benefits, including its ability to neutralize oxidative stress caused by free radicals[1][2][3]. Alkaline water, with its elevated pH level, is widely believed to improve hydration, enhance detoxification, and contribute to overall wellness[4][5]. This has led to its use in various applications such as drinking water, cleaning, and sterilization[6][7][8]. Water ionizers, which alter the pH of water through an electrolysis process, are the primary devices responsible for producing ionized water without adding any chemical or ingredient [9][10][11].

Conventional water ionizers typically utilize expensive electrode materials, such as platinum-coated titanium, to facilitate the electrolysis process [12][13]. While these materials are effective, they significantly increase the cost of the devices, making them less accessible for broader consumer use[14].Additionally, these devices often face challenges such as high energy consumption, limited electrode lifespan, and the risk of metal ion migration, which can compromise the quality and safety of the ionized water, pH stability, and user convenience. In response to these limitations, there is a need for more efficient, cost-effective, and automated systems that can deliver high-quality ionized water with improved performance and reliability[15].

Recent advancements in materials science, particularly in the development of novel electrode materials, have offered new opportunities to overcome these challenges [16]. Graphite-based electrodes, known for their excellent electrical conductivity, chemical stability, and affordability, are emerging as promising alternatives to traditional metal electrodes[17][18][19].In addition to materials innovation, the integration of automation technologies has become increasingly important for improving the user experience and operational efficiency of water ionizers. Modern devices benefit from the incorporation of sensors and control systems that can automatically adjust operational parameters. This automation not only simplifies the user interface but also ensures the consistent production of high-quality ionized water, regardless of variations in input water conditions.

The use of renewable energy sources, such as photovoltaic (PV) solar systems, offers a sustainable solution for powering water ionizers, making them more suitable for eco-conscious consumers and areas with limited access to conventional electricity sources. By harnessing solar power, the energy costs associated with ionization can be minimized, further contributing to the device's overall efficiency and appeal[20].

This research aims to introduce an innovative water ionizer that leverages these advancements by incorporating graphite-based electrodes, an automated control system and a PV solar power supply. The graphite-based electrodes are designed to be a cost-effective alternative to platinum-based electrodes, significantly reducing the overall production cost while enhancing the durability and safety of the ionization process. The integration of an automated control system with pH sensors allows for precise regulation of water pH, delivering consistent results for both alkaline and acidic water production. PV solar system of the ionizer offers a sustainable solution that can operate independently of the electrical grid. The combination of these features results in a low cost, high-efficiency, user-friendly device capable of producing high-quality ionized water for a range of applications.

METHODOLOGY

Device Design

A pre-filtration system was integrated into the device to remove semimetal particles and micro-sized impurities from the water before it enters the electrochemical cell. A 5-micron polypropylene spun cartridge filter was used as a pre-filter. In the electrochemical cell compartment, the filtered water is subjected to an electric current, initiating the ionization process. Polyvinylidene fluoride (PVDF) ion-exchange membranes were used in each electrolysis cell to separate the alkaline and acidic water streams.

Six graphite electrodes (preparation procedure provided below) were configured as both anode and cathode in the electrolysis setup. The ionized water was then directed into two separate chambers: acidic water was collected from the anode side, and alkaline water from the cathode side. A pH regulation chamber was employed to adjust the pH level according to user preferences. The automation of the ionizer was managed by a programmable logic controller (PLC), which regulates essential parameters such as pH selection, flow control, and electrode management. A PH4502C pH sensor and module were placed in the output streams to continuously monitor the pH of the ionized water, allowing for real-time adjustments and precise control of the output. All inputs and outputs were displayed on an LCD screen. The device was powered by a DC power supply, integrated with a silicon (Si) solar panel, a charge controller, and two 12V DC batteries.

Fabrication of Graphite Electrode

Nineteen grams of natural vein graphite (99% purity) purchased (from Kahatagaha Graphite Lanka Ltd) and one gram of phenol-formaldehyde resin (from Glorchem Enterprise)were milled together to obtain a fine and uniform mixture. The mixture was then filled into a specific steel mould and pressed under a compression pressure of 0.8 MPa. The prepared electrode was fired at 180 ± 10 °C for 2 hours. A total of six electrodes were fabricated using the same method. The electrodes were characterized through conductivity measurements before being utilized as electrodes in the electrolysis cells.

Testing and Analysis

Input and output water samples of the water ionizer were analyzed for various parameters using standard test procedures to assess their quality. The parameters tested included pH level, conductivity, and total dissolved solids (TDS). The mineral and heavy metal content of the water was evaluated, focusing on key elements such as calcium, magnesium, sodium, potassium, lead (Pb), cadmium (Cd), arsenic (As), mercury (Hg), chromium (Cr), nickel (Ni), copper (Cu), zinc (Zn), aluminum (Al), iron (Fe), manganese (Mn), phenolic compounds, and selenium (Se). All these tests were performed according to the APHA standard in accredited lab at Industrial technology Institute.

RESULTS AND DISCUSSION

The water ionizer was designed with an integrated pre-filtration system, electrolysis cells, two collection chambers, a pH regulation chamber, automated control mechanisms, and a PV solar power system. The schematic diagram of the overall process is shown in Figure 01.

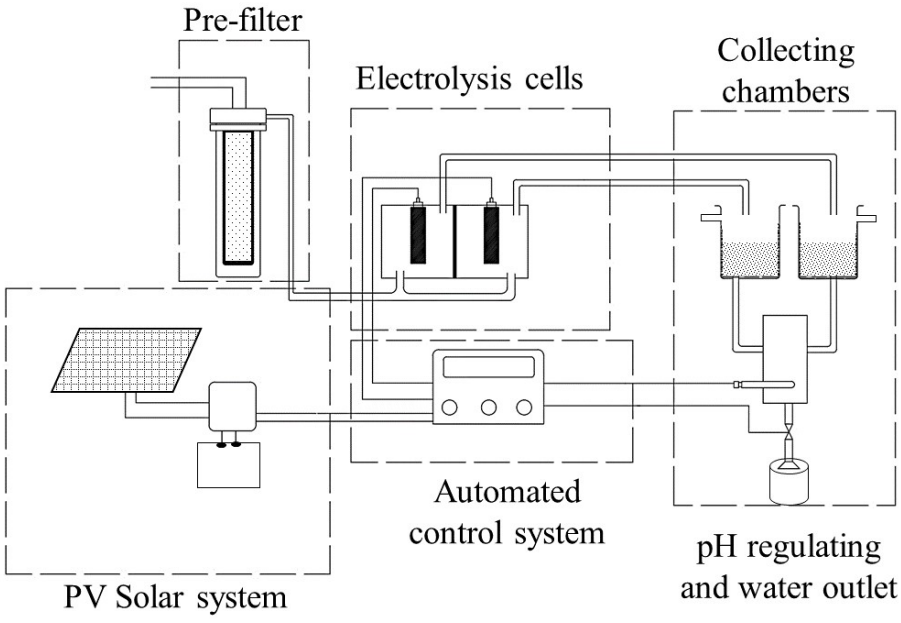

Figure 1. Schematic representation of the water ionizer's overall design and layout, showcasing key components and system architecture.

The device is equipped with a pre-filtration system that serves as the first line of treatment for the incoming water. Specifically, this system utilizes a cartridge filter capable of removing micro-sized

particles lager than 5 microns from the water before it enters the electrolysis chamber. This pre-treatment step ensures that the water entering the ionization process is free from impurities, which helps to maintain the efficiency of the electrolysis process and prolongs the lifespan of the electrodes.

Figure 02 indicates the core of the ionization process occurs in the electrolysis chamber. The anode and cathode electrodes are placed inside the cells.

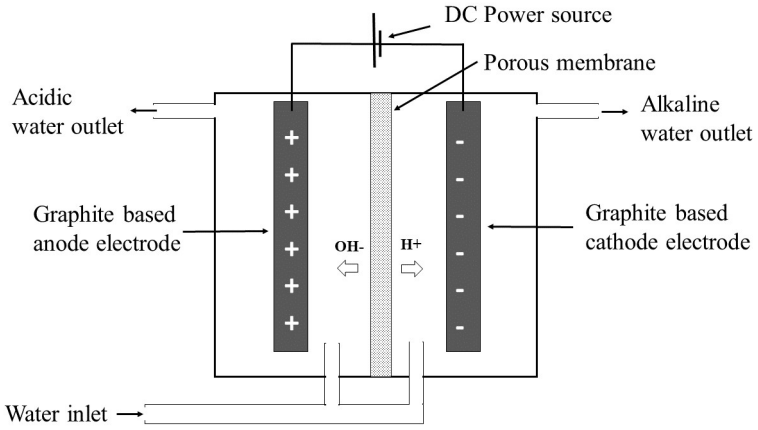

Figure 2. Diagram of the electrolysis process within the ionizer.

These membranes ensure the selective passage of ions, allowing for the separation of positively and negatively charged ions to generate both alkaline and acidic water streams [21]. The multi-cells configuration enhances the efficiency and precision of the ionization process, facilitating better control over the pH levels of the produced water[22]. Within the electrolysis chamber, six graphite-based electrodes acting as anode and cathode are strategically positioned to optimize the electrolysis process. These electrodes consist of a mixture of high-purity graphite (99 %), combined with a resin binder. This composition provides an optimal balance between conductivity, mechanical strength, and chemical stability, making the electrodes both cost-effective and durable. Figure 03 shows the graphite-based electrodes with high electrical conductivity.

Figure 3. The graphite-based electrode used in the ionizer.

Conductivity measurements showed consistent values of approximately 1950 S/m across all six fabricated electrodes, indicating uniform electrode quality. This choice of material reduces the risk of metal ion migration into the water, thus ensuring the safety and quality of the ionized water. These electrodes are connected to the controlling system.

The water ionizer device includes two separate collecting chambers that serve to store the produced alkaline water coming from cathode and acidic water coming from anode preventing cross-contamination between the alkaline and acidic water. The regulating chamber is designed to provide the desired pH level of water by mixing the separated ionized water from the collecting chambers according to the user's request. This chamber continuously monitors the pH levels of water streams, adjust the pH levels as needed through the automated control mechanism. Additionally, each collecting chamber is fitted with a dedicated drain line to dispose of excess water flow, ensuring stable operation and preventing overflow. Figure 04 shows the automated control mechanism which use a key feature of the device, designed to simplify operation while maximizing efficiency. It includes pH sensors that provide real-time feedback to the control system, enabling automatic adjustments of the pH levels. This automation allows the device to maintain stable pH levels, adapt to variations in input water quality, and optimize energy consumption, providing a user-friendly experience.

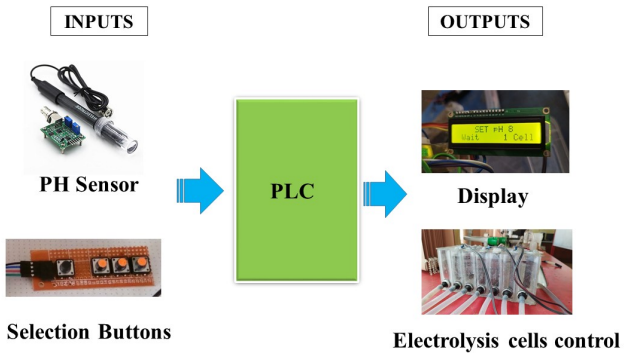

Figure 4. Configuration of the programmable logic control (PLC) system utilized to automate the ionization process, including control features and monitoring capabilities for precise pH adjustments.

To enhance the device's sustainability and applicability in remote or off-grid locations, the ionizer is powered by a silicon (Si) solar panel, a charge controller, and two 12V DC batteries. This system allows the device to operate independently from conventional power sources by utilizing solar energy. Solar panels convert sunlight into electricity, which powers the electrolysis process, thus reducing the reliance on grid electricity and minimizing energy costs. The use of solar power not only aligns with eco-friendly principles but also ensures continuous operation in regions with limited access to stable electricity supplies. Figure 05shows an overview of the key components of the developed water ionizer device.

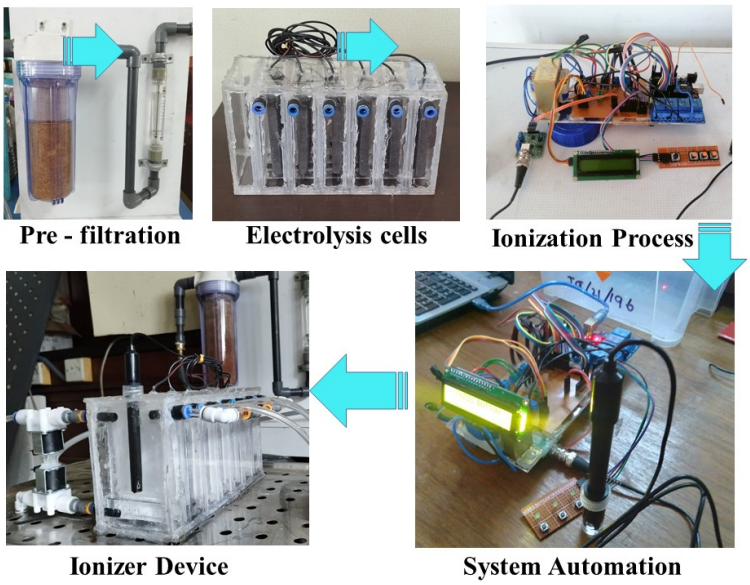

Figure 5. Flowchart depicting each sequential step in the water ionization process, from pre-filtration to final pH-regulated output.

It includes sequential configuration in water ionization, highlighting the importance of each component in achieving efficient and effective ionization. Figure 06 shows the change in pH levels over time during a typical trial using the automated water ionizer.

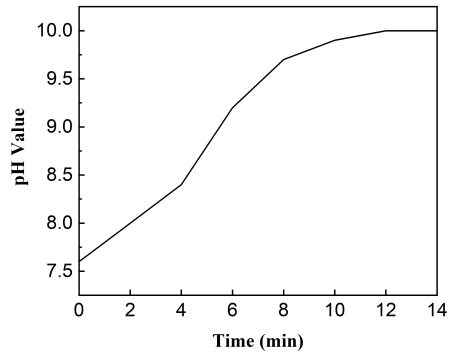

Figure 6: Graph displaying the change in pH levels over time during a typical trial with the automated water ionizer, indicating system stability and efficiency in achieving desired pH levels.

The pH of the water increases from an initial value of approximately 7.0 to around 10.0 within 12 minutes. This trend indicates the efficiency of the ionization process in raising the pH to a desired alkaline level. The steady rise in pH during the initial 10 minutes suggests that the electrolysis system and the graphite-based electrodes are effectively facilitating ion separation and production of hydroxide ions. After 12 minutes, the pH stabilizes near 10.0, indicating that the ionizer has reached a steady-state condition where

the output matches the desired pH range for alkaline water production. This stability demonstrates the capability of the device's control mechanisms, including the pH sensors and PLC system, to maintain the target pH with minimal deviation. The gradual pH increase and eventual stabilization

highlight both the reliability and precision of the system in generating alkaline water for potential applications.

The performance of the high-efficiency water ionizer was evaluated by comparing the properties of inlet and outlet water samples, as summarized in Table 1.

Table 1. Properties of inlet and outlet water samples

	Unit	Inlet Result	Outlet Result
pH at 25°		7.4	8.4
Electrical Conductivity at 25°C	µS/cm	71	73
Total Dissolved Solids at 180°C	mg/L	41	45
Calcium (as Ca)	mg/L	5.1	5.1
Magnesium (as Mg)	mg/L	0.9	0.9
Sodium (as Na)	mg/L	3.5	3.6
Potassium (as K)	mg/L	1.0	1.0
Aluminum (as Al)	mg/L	0.02	0.02
Lead (Pb)	mg/L	ND	ND
Cadmium (Cd)	mg/L	ND	ND
Arsenic (As)	mg/L	ND	ND
Mercury (Hg)	mg/L	ND	ND
Chromium (Cr)	mg/L	ND	ND
Nickel (Ni)	mg/L	ND	ND
Copper (Cu)	mg/L	ND	ND
Zinc (Zn)	mg/L	ND	ND
Iron (Fe)	mg/L	ND	ND
Manganese (Mn)	mg/L	ND	ND
Selenium (Se)	mg/L	ND	ND
Phenolic compounds	mg/L	ND	ND

ND – Not Detected

The pH of the outlet water was measured at 8.4, an increase from the inlet pH of 7.4, indicating effective alkalization. This increase in pH suggests that the ionizer successfully modifies the water's composition to produce alkaline water, a characteristic associated with potential health benefits. Additionally, a slight rise in electrical conductivity was observed, from 71 µS/cm in the inlet to 73 µS/cm in the outlet, along with an increase in total dissolved solids (TDS) from 41 mg/L to 45 mg/L. These minor changes may be due to the increase in ion concentration in the outlet water as a results of the ionization process, which contributes to its enhanced alkalinity and mineral content.

The concentrations of essential minerals, including calcium, magnesium, sodium, and potassium, were found to remain relatively stable. For instance, sodium increased only marginally from 3.5 mg/L to 3.6 mg/L, while the levels of calcium and magnesium showed no measurable change. This stability demonstrates that the ionizer preserves the water's naturally occurring beneficial minerals, ensuring nutrient content remains suitable for consumption. Importantly, all tested

heavy metals and toxic elements, including lead, arsenic, cadmium, mercury, and chromium, were not detected in both inlet and outlet samples. This indicates that the ionizer does not introduce any harmful heavy metal contaminants into the water. The aluminum concentration remained consistent at a low level of 0.02 mg/L, suggesting that the device's components do not contribute to metal leaching. The consistent absence of heavy metals and toxic elements confirm that the device is safe and suitable for producing alkaline water drinking purpose.

CONCLUTION

This study successfully developed and automated a high-efficiency water ionizer, capable of producing ionized water with precisely controlled pH levels through an advanced electrolysis process. The ionizer's ability to generate both alkaline and acidic water makes it suitable for various applications, including sterilization, cleaning, and drinking. The integration of innovative graphite-based electrodes and selective ion-exchange membranes significantly enhanced the accuracy in pH regulation, providing a more reliable and user-friendly experience. Moreover, the inclusion of pH sensors and automated control mechanisms enabled real-time monitoring and adjustments, ensuring consistent output quality. The use of a solar-powered energy system further emphasizes the sustainability of the ionizer, reducing its reliance on traditional power sources and supporting environmental goals.

ACKNOLOWLEDGEMENT

Financial support from the Sri Lanka Treasury (Grant No. TG/21/196)is highly appreciated.

REFERENCE

[1] R.M.C. Ignacio, K.-B. Joo, K.-J. Lee, Clinical effect and mechanism of alkaline reduced water, J. Food Drug Anal. 20 (2012) 33.

[2] F.S.L.G. Delos Reyes, A.C.C. Mamaril, T.J.P. Matias, M.K. V Tronco, G.R. Samson, N.D. Javier, A. Fadriquela, J.M. Antonio, M.E.J. V Sajo, The search for the elixir of life: On the therapeutic potential of alkaline reduced water in metabolic syndromes, Processes 9 (2021) 1876.

[3] J.A. Koufman, N. Johnston, Potential Benefits of pH 8.8 Alkaline Drinking Water as an Adjunct in the Treatment of Reflux Disease, Ann. Otol. Rhinol. Laryngol. 121 (2012) 431–434. https://doi.org/10.1177/000348941212100702.

[4] S. Lal, A.K. Kakodia, S.K. Verma, Alkaline water and human health: Significant hypothesize, J. Appl. Sci. Educ. 2 (2022) 1–11.

[5] B. Benelam, L. Wyness, Hydration and health: a review, Nutr. Bull. 35 (2010) 3–25.

[6] Y.-R. Huang, Y.-C. Hung, S.-Y. Hsu, Y.-W. Huang, D.-F. Hwang, Application of electrolyzed water in the food industry, Food Control 19 (2008) 329–345.

[7] J.-M. Kim, K. Yokoyama, Effects of Alkaline lonized Water on Spontaneously diabetic, Korean J. Lab Anim. Sci I3 2 (1997) 187–190.

[8] C.N. Tango, M.S. Hussain, D.-H. Oh, Application of electrolyzed water on environment sterilization, Electrolyzed Water Food Fundam. Appl. (2019) 177–204.

[9] T.W. LeBaron, R. Sharpe, K. Ohno, Electrolyzed–reduced water: Review ii: Safety concerns and effectiveness as a source of hydrogen water, Int. J. Mol. Sci. 23 (2022) 14508.

[10] J. Chycki, A. Kurylas, A. Maszczyk, A. Golas, A. Zajac, Alkaline water improves exercise-induced metabolic acidosis and enhances anaerobic exercise performance in combat sport athletes, PLoS One 13 (2018) e0205708.

[11] S.M. Ostojic, M.D. Stojanovic, Hydrogen-rich water affected blood alkalinity in physically

active men, Res. Sport. Med. 22 (2014) 49–60.

[12] J. Roller, Low platinum electrodes for proton exchange fuel cells manufactures by reactive spray deposition technology, (2009).

[13] L.K. Abeykoon, H.-Y. Tan, C.-F. Yan, J. Bandara, Significant role of the initial precursor sulfur concentration in the photoelectrochemical hydrogen production of Cu2ZnSnS4 photocathode prepared by thermal evaporation, J. Nanophotonics 16 (2022) 1–15. https://doi.org/10.1117/1.jnp.16.016001.

[14] K.R. Rasmi, S.C. Vanithakumari, R.P. George, U. Kamachi Mudali, Synthesis and characterization of nanostructured platinum coated titanium as electrode material, J. Mater. Eng. Perform. 23 (2014) 1673–1679.

[15] P. Vadthya, N. Thummalapalli, S. Sundergopal, Ultrafiltration membrane assisted cost effective ionizer for production of therapeutic alkaline ionized water, J. Water Process Eng. 32 (2019) 100951.

[16] H. Girault, B. Liu, L. Qiao, H. Bi, M. Prudent, N. Lion, M. Abonnenc, Electrochemical reactions and ionization processes, Eur. J. Mass Spectrom. 16 (2010) 341–349.

[17] R.E. Panzer, P.J. Elving, Nature of the surface compounds and reactions observed on graphite electrodes, Electrochim. Acta 20 (1975) 635–647.

[18] S. Laschi, I. Palchetti, G. Marrazza, M. Mascini, Innovative electrodes to control trace metal ionization used to treat pathogens in water distribution systems, in: Sensors Microsystems AISEM 2011 Proc., Springer, 2012: pp. 25–30.

[19] A.M.K.L. Abeykoon, R.C.L. De Silva, L.D.C. Nayanajith, I.R.M. Kottegoda, A review on appropriate graphene synthesis methods for diverse applications, Sri Lankan J. Phys. 23 (2022) 125. https://doi.org/10.4038/sljp.v23i2.8116.

[20] A. Abeykoon, G. Aponsu, H. Gunathilaka, H.A.V. Nadeera, Effect of temperature on the photovoltaic characteristics of polycrystalline silicon solar cells at hambantota solar power plant, Sol. Asia (2018).

[21] C. Klaysom, B.P. Ladewig, G.Q.M. Lu, L. Wang, Preparation and characterization of sulfonated polyethersulfone for cation-exchange membranes, J. Memb. Sci. 368 (2011) 48–53.

[22] R. Guan, H. Zou, D. Lu, C. Gong, Y. Liu, Polyethersulfone sulfonated by chlorosulfonic acid and its membrane characteristics, Eur. Polym. J. 41 (2005) 1554–1560.

ISSN 1391-0256

Journal of the Sri Lanka Association for the Advancement of Science

Volume 7 Issue 1

9771391025002

Edited and Published by the Sri Lanka Association of for the Advancement of Science

ISSN 1391-0256